Ocean Modelling 31 (2010) 9–27

Contents lists available at ScienceDirect

Ocean Modelling

journal homepage: www.elsevier.com/locate/ocemod

Solitary wave generation dynamics at Luzon Strait

A. Warn-Varnas [a,*], J. Hawkins [b], K.G. Lamb [c], S. Piacsek [a], S. Chin-Bing [a], D. King [a], G. Burgos [d]

[a] Naval Research Laboratory, Stennis Space Center, MS 39529, USA
[b] Planning Systems Inc., Slidell, LA 70458, USA
[c] University of Waterloo, Waterloo, Ont., Canada N2L 3G1
[d] University of Puerto Rico, San Juan 00936, Puerto Rico, USA

ARTICLE INFO

Article history:
Received 27 October 2008
Received in revised form 11 August 2009
Accepted 14 August 2009
Available online 27 August 2009

Keywords:
Nonhydrostatic model
Tides
Solitary waves
Dispersion
Near surface shear
Generation dynamics
Parameter variation

ABSTRACT

A high resolution modeling study is undertaken, with a 2.5-dimensional nonhydrostatic model, of the generation of internal waves induced by tidal motion over the ridges in Luzon Strait. The model is forced by the barotropic tidal components K1, M2, and O1. These tidal components, along with the initial density field, were extracted from data and models. As the barotropic tide moves over the Luzon Strait sills, there is a conversion of barotropic tidal energy into baroclinic tidal energy. Depressions are generated that propagate towards the Asian Seas International Acoustics Experiment (ASIAEX) test site on the Chinese continental shelf. Nonlinear effects steepen the depressions, frequency and amplitude dispersion set in, and disintegration into large amplitude solitary waves occurs. The effects of varying the initial density field, tidal component magnitudes, as well as adding a steady background current to represent the occasional excursions of the Kuroshio Current into the strait, are considered.

Depressions are generated at each of the two sills in Luzon Strait which radiate away, steepening and evolving into internal solitary wave trains. Baroclinic fluxes of available potential energy, kinetic energy and linear are calculated for various parameter combinations. The solitary wave trains produced in the simulations generally consist of large amplitude wave trains alternating with small amplitude wave trains. During strong tidal flow, Kelvin–Helmholtz type instabilities can develop over the taller double-humped sill. The solitary waves propagating towards the ASIAEX test site have been observed to reach amplitudes of 120–250 m, depending on the tidal strength. ASIAEX observations indicate amplitudes up to 150 m and the Windy Island Experiment (WISE) measurements contain magnitudes over 200 m. The model results yield solitary wave amplitudes of 70–300 m and half widths of 0.60–3.25 km, depending on parameter values. These are in the range of observations. Measurements by Klymak et al. (2006), in the South China Sea, exhibit amplitudes of 170 m, half widths of 3 km and phase speeds of 2.9 $m\,s^{-1}$. Model predictions indicate that the solitary waves making up the wave packet each experience different background currents with strong near surface shear.

The energy in the leading soliton of the large amplitude wave trains ranges between 1.8 and 9.0 $GJ\,m^{-1}$. The smaller value, produced using barotropic tidal currents based on the Oregon State University data base, is the same as the energy estimated to be in a solitary wave observed by Klymak et al. (2006). Estimates of the conversion of barotropic tidal energy into radiating internal wave energy yield conversion rates ranging between 3.6% and 8.3%.

Published by Elsevier Ltd.

1. Introduction

In recent years satellite SAR measurements of several oceanic areas have revealed the surface signatures of propagating internal solitary-like waves (ISWs). These waves have been found to have particularly large amplitudes and propagation speeds in the Andaman and Sulu Seas around the Indonesian Archipelago (up to 90 m and 1.8 $m\,s^{-1}$ respectively) Osborne and Burch, 1980, 1985. Larger amplitude waves have been observed in the South China Sea propagating away from Luzon Strait where waves with amplitudes ranging from 100 to 170 m and wave induced currents between 1.8 and 2.4 $m\,s^{-1}$ have been observed (Liu et al., 1985, 2004,, 2006). Even larger waves were observed in the South China Sea during the Windy Island Soliton Experiment (WISE) which measured wave amplitudes of up to 250 m and phase speeds of around 3.4 $m\,s^{-1}$ Ramp, 2006. Recent studies and measurements have shown that these ISWs exert a profound influence on the acoustic transmission of signals in the 400–600 Hz range Zhou et al., 1991, 2004,.

* Corresponding author. Address: Naval Research Laboratory, Code 7322, Bld. 1009, Stennis Space Center, MS 39529, USA. Tel.: +1 228 688 5223; fax: +1 228 688 4759.
E-mail address: varnas@nrlssc.navy.mil (A. Warn-Varnas).

1463-5003/$ - see front matter Published by Elsevier Ltd.
doi:10.1016/j.ocemod.2009.08.002

Past numerical simulations of ISWs have included studies of waves appearing in the Sulu Sea Liu et al., 1985,, shelf zones of Guinea and Morocco Vlasenko, 1993, 1996, the Strait of Gibraltar Brandt et al., 1996, and the Strait of Messina Brandt et al., 1996, 2003. The Strait of Messina model predictions were compared with data Brandt et al., 1996, 2003, 2007, indicating that models can accurately predict the generation and location of the solitary wave trains. ISW generation in the Yellow Sea, including studies of the effects of the waves on acoustic propagation, has also been simulated Warn-Varnas, 2002, 2003, 2005, 2006. Numerical studies of ISW generation by tidal flow over the ridges in Luzon Strait have also been performed Niwa and Hibiya, 2004, 2002, 2007.

The recent large field experiment ASIAEX has generated much interest in furthering our understanding of the generation and evolution of the large amplitude solitary waves observed in the South China Sea. Various analyses of the SAR surface signatures of the moving waves, including their direction of propagation, and of the time series of the current and temperature data at moorings and CTD casts, have led to the conclusion that these waves are largely generated by the barotropic tide moving over the large sills in Luzon Strait between Taiwan and Mindanao, and on the slope region of the northern boundary of the South China Sea (SCS). Depressions are generated at the Luzon Strait sills which propagate towards the ASIAEX test site on the Chinese continental shelf. Nonlinear effects steepen these depressions until they become dispersive and they disintegrate into ISWs of large amplitude. Zhao and Alford (2006) related the ISWs observed near Dongsha Island to tidal currents passing through Luzon Strait, finding that westward flow through the strait was responsible for the generation of ISW packets.

In this paper we model the ISW generation process associated with tidal flow through Luzon Strait. An idealized 2.5D model is used with topography, tidal forcing and stratification based on observations. The use of a 2.5D model makes it feasible to perform high resolution simulations to accurately simulate the generation of ISW trains. The sensitivity of the results to the initial density profile, the amplitudes and phases of the various tidal components, and to an imposed background current that represents the influence of Kuroshio excursions into the SCS through Luzon Strait, is explored.

Section 2 describes the model and the simulation setups. In Section 3 the wave generation process is described and discussed, first as to the general characteristics of the generation and propagation processes as revealed by the numerical results, and then as to the effects of imposed background flow and parameter variations. Section 4 contains dispersion analysis, Section 5 comparison with measurements and analytical solutions, and conclusions are presented in Section 6.

2. Model

2.1. Equations

A 2.5-dimensional fully nonhydrostatic model is used for simulating the generation and propagation of internal solitary waves Lamb, 1994. Flow in the along ridge y-direction is included but the flow is independent of y, hence the designation "2.5-dimensional". The model uses the rigid-lid, traditional f-plane, Boussinesq and incompressible flow approximations. The governing equations are

$$\vec{U}_t + \vec{U}\cdot\nabla\vec{U} - f\vec{U}\times\hat{k} = -\frac{1}{\rho_0}\nabla p - \frac{\rho}{\rho_0}g\hat{k}, \tag{1}$$

$$\rho_t + \vec{U}\cdot\nabla\rho = 0, \tag{2}$$

$$\nabla\cdot\vec{U} = 0. \tag{3}$$

Here ρ is the density, ρ_0 the reference density, p the pressure and $\vec{U} = (u, v, w)$ is the velocity field with components in the (x, y, z) directions, where z is the vertical coordinate, the horizontal x-coordinate is directed across the topography and y is along the topography. ∇ is the 3-dimensional vector gradient operator, however all fields are independent of y. The subscript t denotes differentiation with respect to time. There are two fixed parameters, namely the gravitational acceleration $g = 9.81\ \mathrm{m\,s^{-2}}$ and the Coriolis parameter $f = 5.2\times10^{-5}\ \mathrm{s^{-1}}$ corresponding to a latitude of 21° N. $\hat{k}$ is the unit vector in the z-direction. These simulations do not use explicit viscosity and diffusion terms. The model uses flux limiting which acts to control the overturns that occur in the simulations. In the ocean strong mixing can be expected over the sill and this will of course have an influence on the internal waves which are generated. A proper account of this is an important problem for the future. At the resolutions used here numerical dispersion and dissipation is negligible for the radiating internal tide and solitary waves. Numerical dissipation and dispersion have not caused noticeable deviation in predicted soliton amplitudes and wavelengths in relation to data Warn-Varnas et al., 2007.

Fig. 1 shows the bathymetry in the Luzon Strait-SCC region. The topography through Luzon Strait used in the simulations was obtained from the Digital Bathymetric Data Base with a 5 min resolution (DBDB5) along track 1 in Fig. 1. In Luzon Strait there are two large double-humped sills which are believed to be the primary internal wave generation sites. Away from the sills we have set the ocean floor to a depth of 3665 m. The largest peaks of the two sills rise to depths of about 1850 and 650 m (see Fig. 4(b)). The smaller, western-most sill will be referred to as the first sill. Once the solitary waves are generated, they are not affected by deep topography variations. They are ultimately strongly affected by the shoaling topography on the western side of the SCC, however we have not simulated this process in this study. Before the equations are solved, they are transformed to a terrain following coordinate system which leads to higher vertical resolution over the sills in Luzon Strait. For most simulations the numerical grid consists of 14,400 grid points in the horizontal and 100 grid points in the vertical. The grid is stretched in the horizontal with a 70 m resolution in a 900 km long central domain lying between $x = -650$ and 250 km. The horizontal resolution smoothly increases to 1000 m beyond this central region of interest. In the vertical sigma coordinates are used. The vertical resolution varies from 6 m over the taller sill to 36.65 m away from the sills. The time step of the simulations is subject to a CFL condition and varies throughout the simulation. It ranges from 1 to 5 s. For some simulations the resolution was doubled (see Section 3.6).

2.2. Tidal variability and model forcing

At latitude 20.79 N and longitude 120.94 E, the location of a previous experimental mooring site (Table 1 and Fig. 1), the Oregon State University (OSU) data base yields the barotropic tidal components shown in Fig. 2 for Julian days 110–150 of 2001. A diurnal and semidiurnal component is evident with a superposed fortnightly-modulated envelope which exhibits a maximum and a minimum every 15 days. The east–west velocity u is larger that the north–south velocity v.

The corresponding barotropic velocities, as extracted from the Naval Coastal Ocean Model (NCOM) that contains tidal forcing, are also shown in Fig. 2. The components show a structure similar to the OSU data base components. The magnitude of the NCOM components are, however, larger by up to a factor of 2.1.

The variability of the barotropic tide in the Luzon Strait region is shown in Fig. 3. Here the along-track horizontal barotropic currents extracted from the OSU data base are shown at the experimental mooring site and at four locations ('moorings' 1–4) along

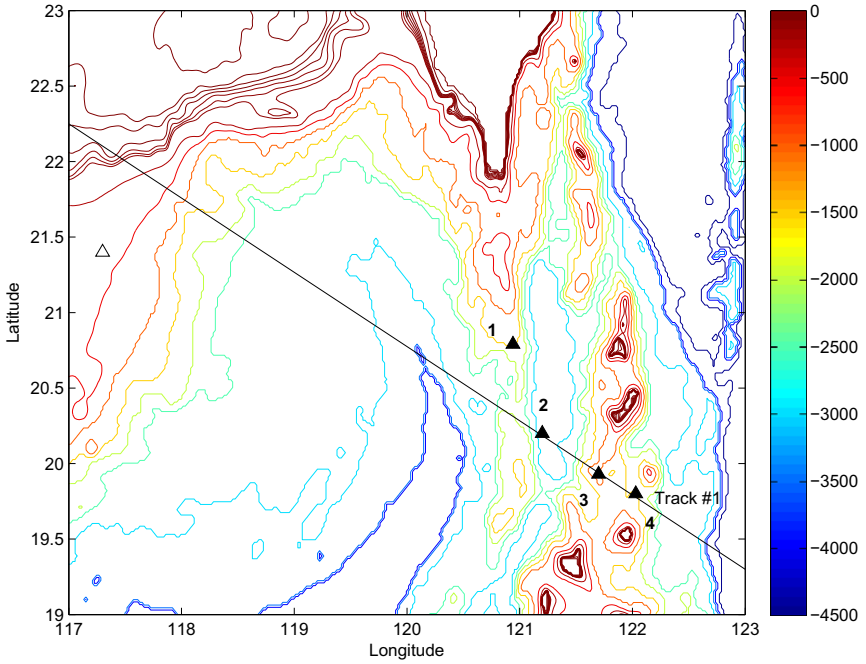

Fig. 1. Luzon Strait and South China Sea region. Track 1 is the section along which 2-dimensional modeling is performed. Black triangles indicate mooring locations. Latitudes and longitudes of moorings introduced into model domain (1 through 4) indicated by black triangles are listed in Table 1. White triangle indicates ASIAEX S7 mooring.

Table 1
Mooring locations in Luzon Strait-SCC region.

Mooring	Location	Depth (m)
1	20.79 N, 120.94 E	1408
2	20.20 N, 121.20 E	3554
3	19.93 N, 121.70 E	913
4	19.80 N, 122.03 E	1228

the track through Luzon Strait. The latitudes and longitudes of all moorings are listed in Table 1. A fortnightly amplitude modulation and the diurnal and semidiurnal components are visible at all the mooring sites, and the maximums and minimums of the u velocity are in phase, indicating tidal coherence along the track. The magnitude of the u velocity component decreases with depth as a result of volume flux conservation.

In the numerical simulations the u-component of tidal velocity at the left boundary $(x = x_L)$ has the form

$$u(x_L,z,t) = A_{K1}\sin(\omega_{K1}t+\phi_{K1}) + A_{M2}\sin(\omega_{M2}t+\phi_{M2}) + A_{O1} \times \sin(\omega_{O1}t+\phi_{O1}). \quad (4)$$

Here A, ω and ϕ are the amplitude, frequency and phase of the K_1, M_2 and O_1 tidal components, as indicated by the subscript. Table 2 lists the tidal forcing amplitudes and phases that are used in the simulations, these values being based on the OSU data base and NCOM values adjusted to the 3665 m depth at the left boundary. T_1 represents tidal components extracted from OSU data base at mooring site 1, T_2 is 2.1 times T_1 and reflects the magnitudes predicted by NCOM at mooring site 1. NCOMs representation of local features with higher regional horizontal resolution yields a higher value for the local tide. T_3 is 4.7 times T_1, and represents a strong tidal forcing magnitude.

2.3. Model initialization

Density profiles to the right (east) and left (west) of Luzon Strait were extracted from the NCOM predictions for April 15, 2001 (Fig. 4(a)). In the model domain the density was interpolated, somewhat arbitrarily, between these two profiles over Luzon Strait yielding the 2D density shown in Fig. 4(b), where the deeper extent of the stratification on the east side is evident. The transition between the two density profiles occurs over the taller sill.

The initial x-component of the velocity field at the left boundary is given by (4) at $t = 0$ from which the vertically uniform initial field throughout the domain is obtained using conservation of volume flux Q. The incompressibility condition then gives the initial vertical velocity field $w = Qzd'(x)/d^2(x)$ where $d(x)$ is the water depth and the prime denotes differentiation. The initial y component of the velocity field is obtained by assuming that v and u are related by $v_t + fu = 0$ (i.e., the initial v is what it would be if the ocean was of constant depth). This gives

$$v(x,z,0) = f\frac{d(x_L)}{d(x)}\left(\frac{A_{K1}}{\omega_{K1}}\cos\phi_{K1} + \frac{A_{M2}}{\omega_{M2}}\cos\phi_{M2} + \frac{A_{O1}}{\omega_{O1}}\cos\phi_{O1}\right). \quad (5)$$

3. Dynamics

A total of seven cases were run, details of which are provided in Table 3. The first five were initialized with the horizontally variable density depicted in Fig. 4, which we denote by stratification ρ_a. For comparison two runs were done using horizontally homogeneous stratifications, one using the stratification to the west of the ridge (case 6) and one using the stratification to the east of the ridge (case 7). The first three cases use the three tidal forcings given in Table 2. Two runs include a background geostrophic flow $U_g(x,z)$ across the ridge, one to the east (case 4) and one to the west (case 5). This is motivated by the occasional excursions of the Kuroshio current through the strait. The geostrophic current U_g is balanced by the addition of a y-independent pressure gradient in the momentum equation for v.

We begin by discussing the first case in detail and then consider how the generation and propagation of the internal solitary wave

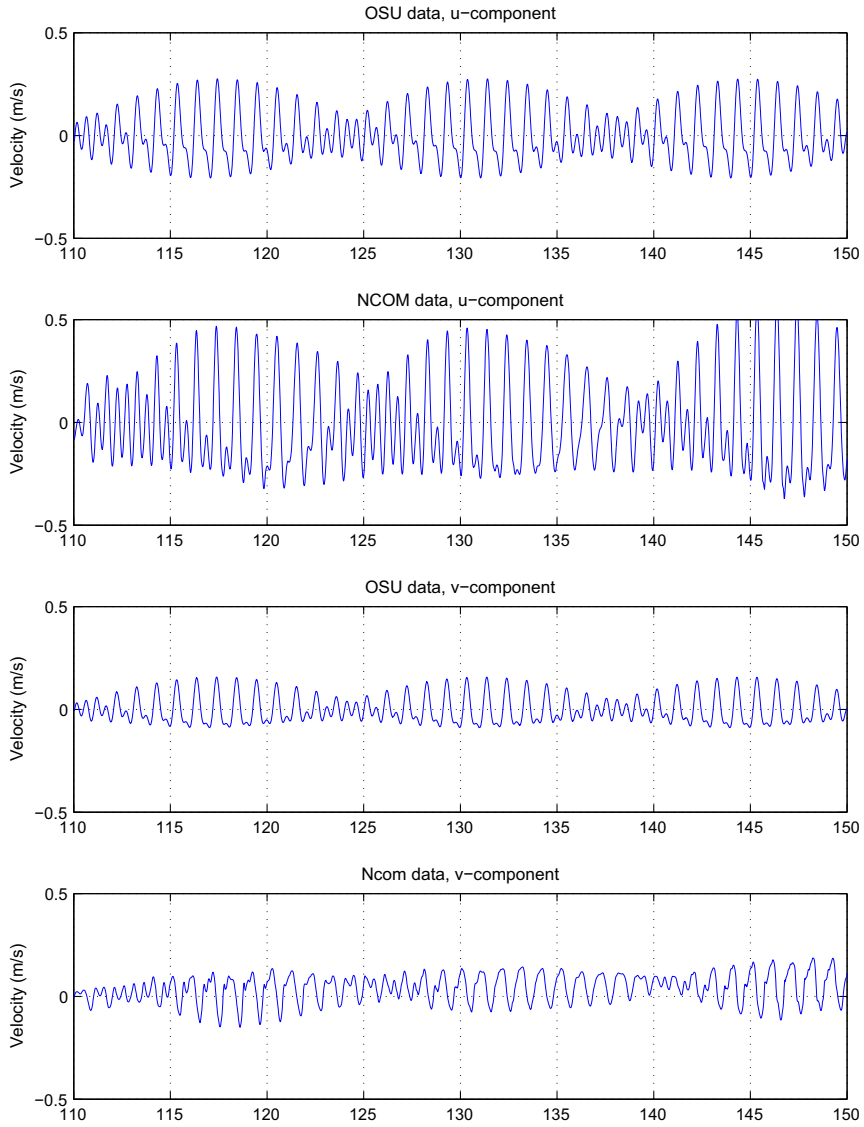

Fig. 2. u and v tidal velocities, along track in Fig. 1, at mooring location 1 in Table 1 for Julian days 110 through 150. From top to bottom the plots are labeled a, b, c, and d. NCOM data is obtained by vertically averaging the baroclinic NCOM predictions.

trains is affected by the amplitude of the barotropic tidal constituents, by a background geostrophic current, and by the density structure. We then discuss the energetics of the solitary wave trains.

3.1. Case 1: the base case

We begin with case 1. Fig. 5 shows the prescribed tidal velocity at the left boundary over a time span of 96 h. The time series uses the tidal components for configuration T_2 listed in Table 2. The density field at six different times is shown in Fig. 6. After 13 h, just past peak westward flow, overturning depressions are visible over the lee of the two peaks of the second sill at about −20 and 40 km (Fig. 6(a)). To the left of these, at about $x = -40$ km, a broader, shallower leftward propagating depression can be seen. This was generated when the depressions first form. As the direction of tidal flow reverses, the large depressions are advected rightward over the sill crests. At $t = 19$ h, at peak rightward flow, large depressions have formed at 10 and 60 km accompanied by stronger overturning (Fig. 6(b)). The depression at 60 km moves off to the right and ultimately evolves into a solitary wave train. Over the first sill there is a long depression between about $x = -130$ and −30 km (Fig. 6(b)). At the second sill there is a large overturning wave near $x = 0$ km.

As the tidal flow reverses again and proceeds to the left, a flat bottom depression of the isopycnals forms. By $t = 24$ h it is centred near −150 km (Fig. 6(c)). As the depression propagates away from the sill, the leading side steepens because of nonlinear effects. Then dispersion sets in and disintegration into solitary-like waves occurs. At 32 h (Fig. 6(d)) the leading edge, at about −300 km, has disintegrated into solitary waves, and another depression is forming at about −100 km from which, by 38 h (Fig. 6(e)), a second solitary wave train has formed. There is a single solitary wave train on the right side at this time. By 66 h (Fig. 6(f)) more solitary wave trains have evolved, with four wave trains to the left of the sills and three to the right. The wave-train at around −500 km, previously located at −200 km (Fig. 6(e)), has evolved into a six solitary wave-train with large amplitude solitary waves in front. The train at −300 km has smaller amplitude solitary waves, while the wave-train that is forming at about −200 km evolves into a large amplitude wave-train. This indicates that large amplitude wave-trains are spaced between smaller amplitude wave-trains. There are fewer wave-trains in the wave trains to the right of the sills and these

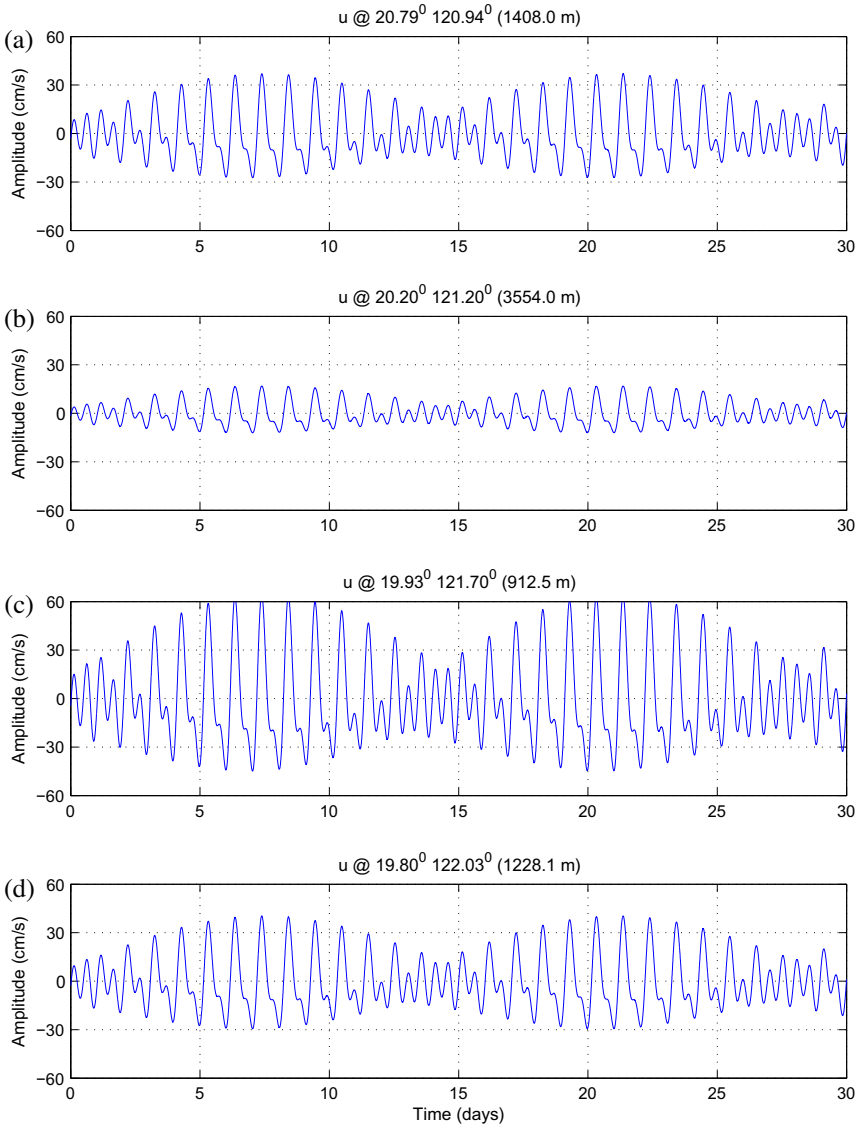

Fig. 3. u component of velocities at the four mooring sites, a through d, listed in Table 1 for 30 days from Julian day 110, 2001. Extractions are from OSU data base.

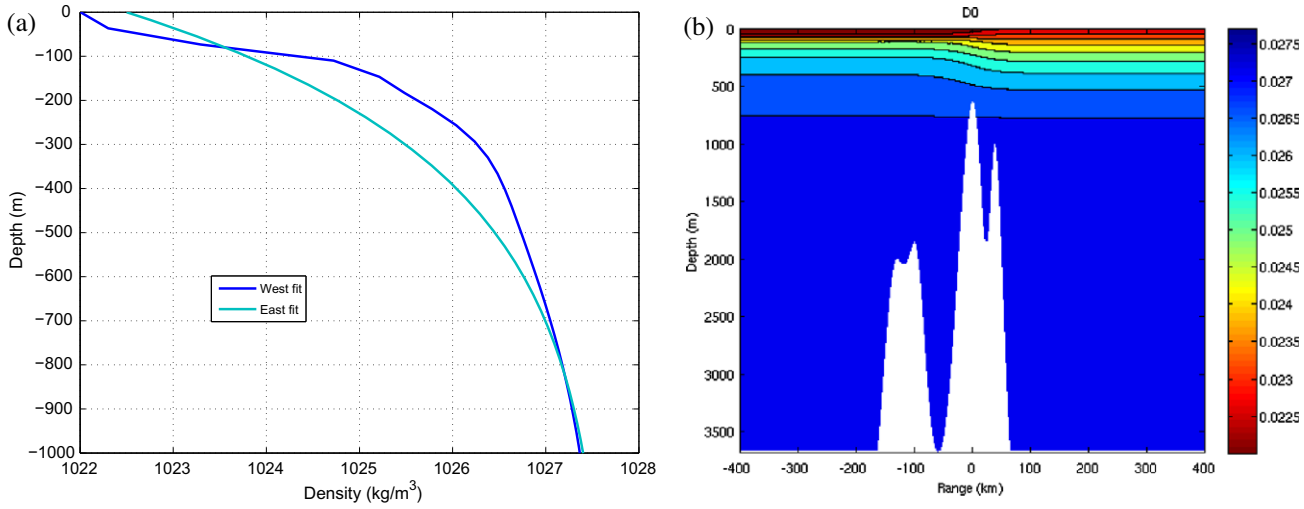

Fig. 4. Initial density field: (a) blue curve is west CTD fit and magenta curve is east CTD fit and (b) Initial density field using interpolated density ρ_a. Topography is extracted along track 1 in Fig. 1 down to a depth of 3665 m. (For interpretation of references in color in figure legends, the reader is referred to the web version of this article.)

Table 2
Amplitude and phase of constituents of tidal forcing at left boundary in model runs.

Tidal forcing	u_{M2} (m s^{-1})	u_{K1} (m s^{-1})	u_{O1} (m s^{-1})	ϕ_{M2} (m s^{-1})	ϕ_{K1} (m s^{-1})	ϕ_{O1} (m s^{-1})
T_1	.0439	.0485	.03330	−1.49	−3.47	+1.46
T_2	.09219	.10185	.07017	−1.49	−3.47	+1.46
T_3	.20633	.228	.15651	−1.49	−3.47	+1.46

Table 3
Stratification, tidal forcing and background geostrophic current for the seven cases. Here ρ_a is an interpolation of ρ_w and ρ_e, ρ_w is the density on the west side ρ_e and is the density on the east side; T_1 through T_3 are tidal configurations, listed in Table 2; U_g is the prescribed background geostrophic velocity at the left boundary (depth 3665 m).

Case	ρ	Tidal forcing	U_g (m s^{-1})
1	ρ_a	T_2	0
2	ρ_a	T_1	0
3	ρ_a	T_3	0
4	ρ_a	T_2	+.1
5	ρ_a	T_2	−.1
6	ρ_w	T_2	0
7	ρ_e	T_2	0

tend to consist of one large solitary wave. The first, second and fourth ISW trains were generated by the peak westward tidal currents over the tallest sill (e.g., at $t = 12, 36, 60$ h, etc.) while the smaller wave trains appear to be generated by flow over the smaller, leftward sill. This was verified by a simulation with the smaller, westward sill removed. This simulation also showed that the presence of the smaller sill enhances the amplitudes of the large solitary wave trains, in contradiction to the finding of Chao et al. (2007) who found that the westward sill acted to decrease the amplitude of the internal tide. The discrepency could be due to differences in the stratifications used and details of the topography. At $t = 66$ h the leftmost wave-train is just reaching the region where the grid stretching begins ($x = -600$ km).

An alternative view of the early stages of the wave generation process is presented in Fig. 7. Here the $\sigma_\theta = 26.74$ isopycnal is shown at 6 h intervals between $t = 12$ and 36 h on the west side of the large sill. This isopycnal has a rest depth of about 500 m on the west side of the strait. For reference, the location of the sills is indicated with a dashed line. At $t = 12$ h, shortly before peak westward tidal flow, there are depressions in the lee of each sill

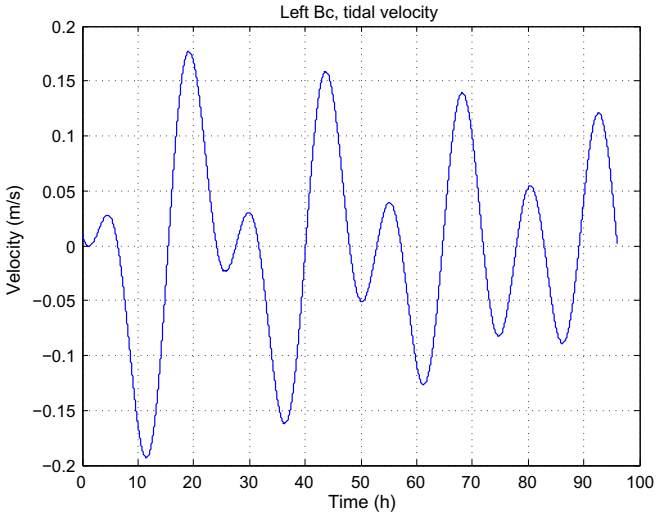

Fig. 5. u component of the tidal velocity at the left boundary.

($x = -140$ and -40 km). Some of the energy in these depressions propagates to the left. At $t = 18$ h the depressions are at $x = -220$ and -100 km. At this time the tidal flow is close to its maximum eastward strength. This has resulted in the raising of the isopycnals above the smaller sill at about $x = -130$ km. Energy is added to the leftward propagating depression by the eastward tidal currents flowing down the lee (right side) of the sill and subsequently the depression passes over the small sill and by $t = 24$ h ISWs are starting to emerge. This depression has now escaped the influence of the topography and the ISW train emerges in the well understood manner. A run done with the smaller sill removed resulted in a leading ISW train of approximately half the amplitude. In addition, the weak depression and elevation seen at $x = -400$ and -320 km at $t = 36$ h were absent. These were formed by the first periods of strong westward and eastward flow over the smaller sill respectively. The early stage of the first large ISW train can be seen at $x = -120$ km at $t = 36$ h. Its generation is somewhat obscure. It forms at the back of a large elevation formed over the larger sill during the first period of strong eastward tidal flow. This large narrow elevation can be seen at about $x = -10$ km at $t = 18$ h. By $t = 24$ h the leftward part of the elevation is very broad, lying between $x = -120$ and -30 km. In the simulation without the smaller sill this wave train was very similar during the late stages of its development. A simulation was done in which the water depth was held constant from the top of the tall sill at $x = 0$ until about $x = 200$ km after which the water depth gradually increased to the initial far field depth. The first three leftward propagating ISW packets were not significantly different indicating that the formation of a depression in the lee of the large sill during eastward flow plays little role in the formation of these wave trains.

3.2. Effects of tidal current strength

The strength of the barotropic tidal currents has a significant impact on the amplitude of the internal waves generated by tide-topography interaction. Indeed, linear theory predicts the internal wave amplitudes are proportional to the tidal amplitude and hence that nonlinear processes are proportional to the square of the tidal forcing. In case 2 the barotropic tidal currents are approximately half of those in case 1. A snapshot of the isopycnals at 66 h is shown in Fig. 8(a). For ease of reference, the corresponding density fields from case 1, shown in Fig. 6(e), are repeated in Fig. 8(b). The solitary wave trains to the right side of Luzon Strait are no longer present. On the left of Luzon Strait, a solitary wave train near $x = -500$ km with two solitary waves has formed. Correspondingly, an increase in tidal forcing, as in case 3, results in larger amplitude waves. The increased tidal magnitude of case 3 results in higher velocities over the sills. At the second taller sill, breaking lee waves occur at 13 h (Fig. 9(a)) and Kelvin–Helmholtz type of instabilities can develop (Fig. 9(b)).

3.3. Background currents seen by ISWs

The properties of ISWs depends on the environment through which they propagate. They depend not only on the stratification but also on background sheared currents. In our simulations, and

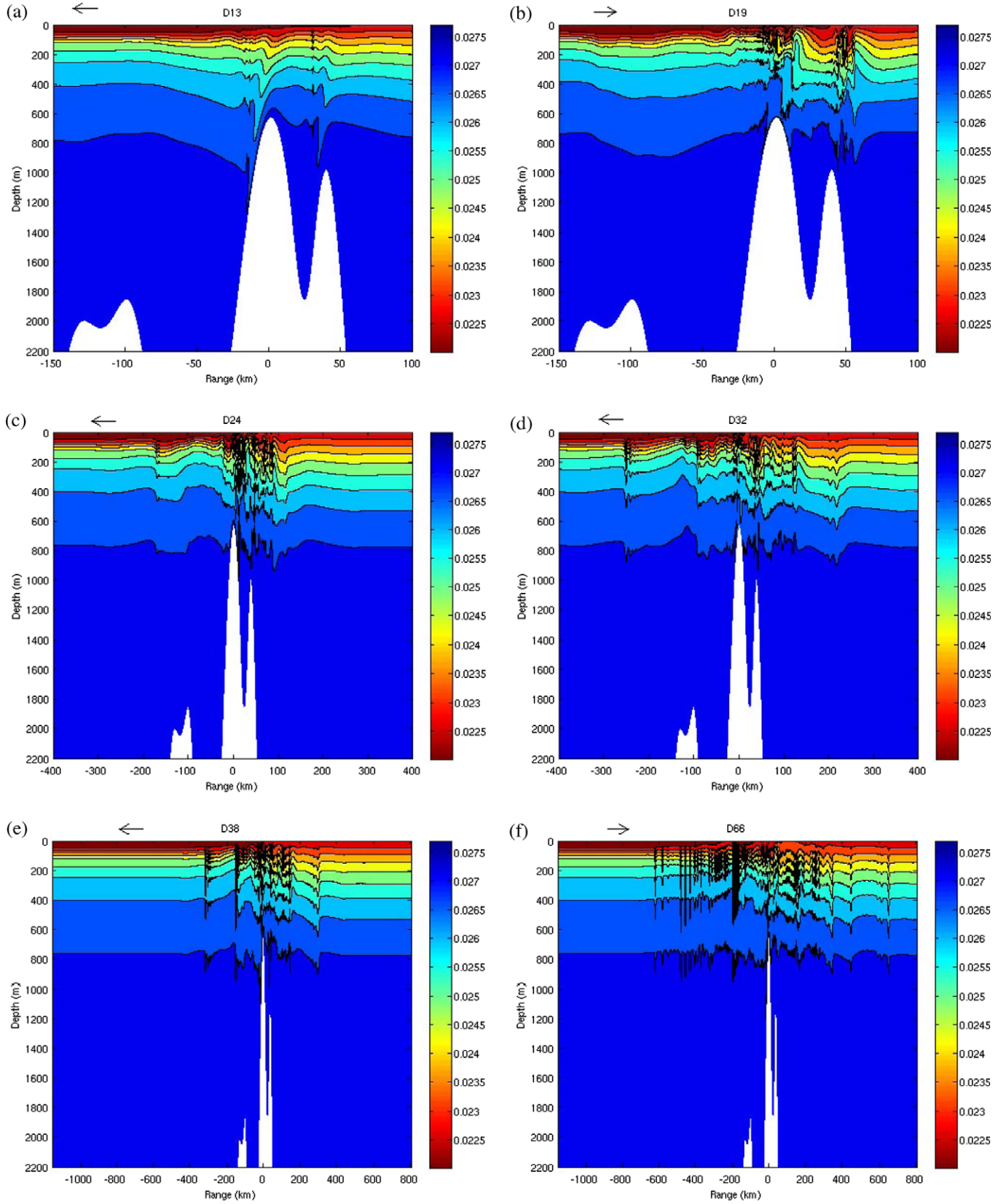

Fig. 6. Simulated density field for case 1: (a) $t = 13$ h, (b) $t = 19$ h, (c) $t = 24$ h, (d) $t = 32$ h, (e) $t = 38$ h and (f) $t = 66$ h. Arrows, on top left, indicate direction of tidal flow.

indeed, in the ocean, the ISWs are not isolated features. They are imbedded in the internal tides generated by the various constituents of the barotropic tide, of which each ISW sees a different part. In addition, rotation causes the ISWs to radiate waves behind them which may effect those which follow Helfrich, 2007. This is illustrated in Fig. 10 which shows the surface velocity at a sequence

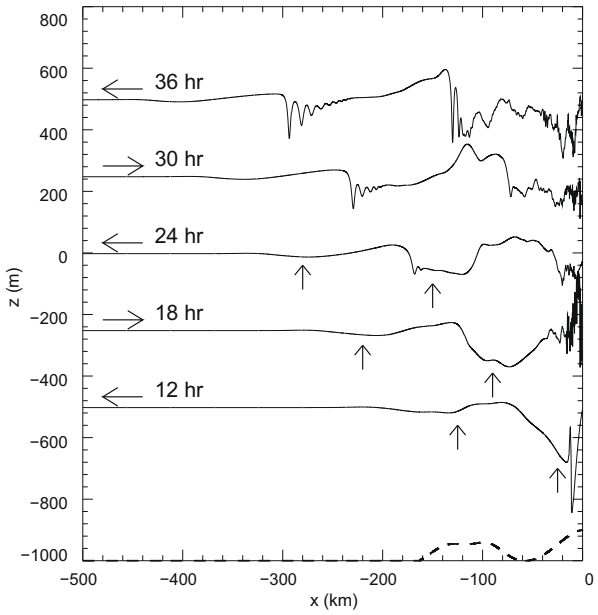

Fig. 7. The $\sigma_\theta = 26.74$ isopycnal from case 1 at 6 h intervals between $t = 12$ (lowest curve) and 36 h (upper curve). The isopycnals after $t = 12$ h are offset by 250 m increments. The dashed lines in the lower right of the plot indicate the location of the two sills. Horizontal arrows on the left side indicate direction of tidal flow. Vertical arrows mark depressions.

of times from a simulation of the evolution of a single ISW. For this simulation a flat bottom domain was used and the model was initialized with a single exact solitary wave ignoring the presence of rotation Lamb, 2002. The simulation was then done in a moving reference frame to minimize the extent of the horizontal domain. Both the presence of the internal tide and rotational effects result in each wave train and, indeed, each individual ISW, experiencing different background conditions. Hence we now briefly explore the background surface currents ahead of the first few ISWs in the first large leftward propagating wave train.

Fig. 11 shows the horizontal velocity at different depths plotted as a function of x for the second leftward-propagating solitary wave train in case 1 at $t = 60$ and 68 h. At 60 h the first ISW is located at about $x = -408$ km. By 68 hr it has propagated to $x = -505$ km. The depths in Fig. 11 range from 50 to 350 m. The wave induced current amplitudes decrease with depth. Fig. 12 shows vertical profiles of the wave-induced currents (barotropic currents removed) at locations ahead of the wave train and between the first and second and third solitary waves. These illustrate that the solitary waves making up the wave packet each experience different background currents which, furthermore, vary in time. In particular at 60 and 68 h these waves experience currents with strong near surface vorticity of the opposite sign to the solitary wave induced vorticity. These currents oppose the motion of solitary waves in the train and influence the resultant location and structure of solitary waves within the train.

3.4. Effects of a geostrophic background current

The Kuroshio normally flows northward along the east side of Luzon Strait with a bend towards the west. Its magnitude is around 1 m s^{-1}. In some years it intrudes to the west side of Luzon Strait in the form of a loop and exits again back to the east side. In either case there can be a component of the Kuroshio along the east–west propagation direction through the strait. To investigate the possible effects of such a current two model runs were done by introducing geostrophic background currents with strengths ± 0.1 m s^{-1} at the left boundary where the water depth is 3665 m (cases 4 and 5). Over the sills they are significantly stronger, having magnitudes of about 0.2 and 0.56 m s^{-1} over the crests of the westward and eastward sills. Case 4 uses an eastward geostrophic current. Fig. 13 shows the predicted density field for this case over the sills at $t = 13$ h, the time of maximum westward tidal flow, and over a longer region at $t = 38$ h. At 13 h the isopycnals have less visible depressions at the taller sill than in the corresponding figure from case 1 (Fig. 6(a)). As expected, an eastward current opposes the generation of internal waves during periods of westward tidal flow. At $t = 13$ h the effect of the background current is to reduce flow over the sills by a factor of two. The surface isopycnals show a square type of wave structure at about −30 km in presence of an eastwards current, with a bimodal structure in the vertical. The square wave forms during the period of westward tidal flow in the presence of an eastward current. At about 40 km another bimodal structure is evident. In the absence of a background current the bimodal structure is less complex (see Fig. 6(a)). At 38 h there is an

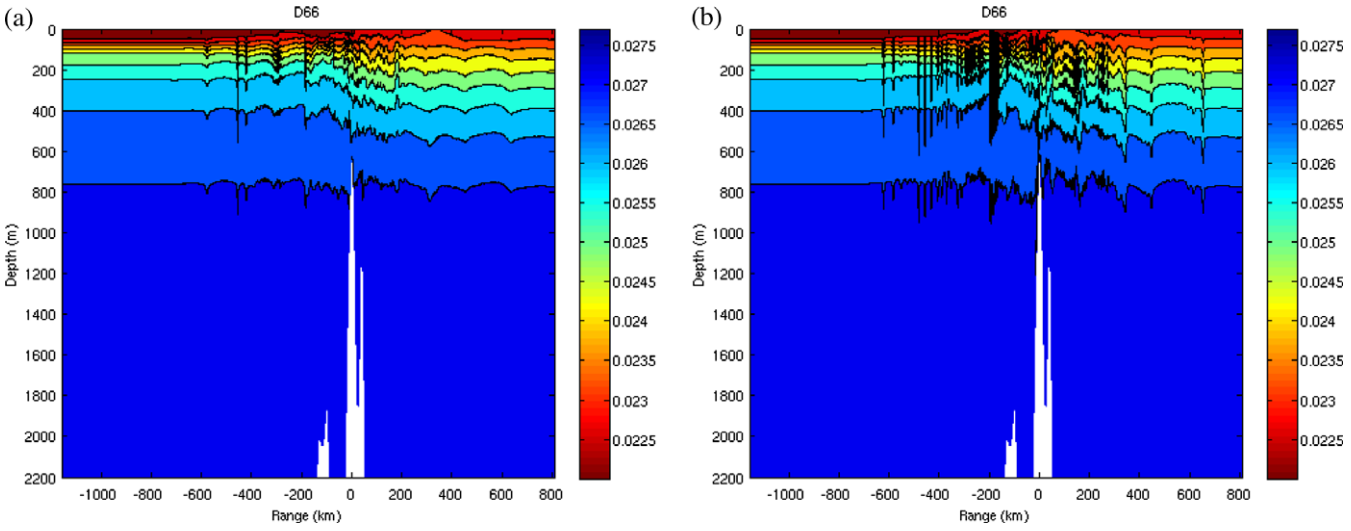

Fig. 8. Density field at 66 h: (a) case 2 (weak tidal currents) and (b) case 1 (intermediate strength tidal currents).

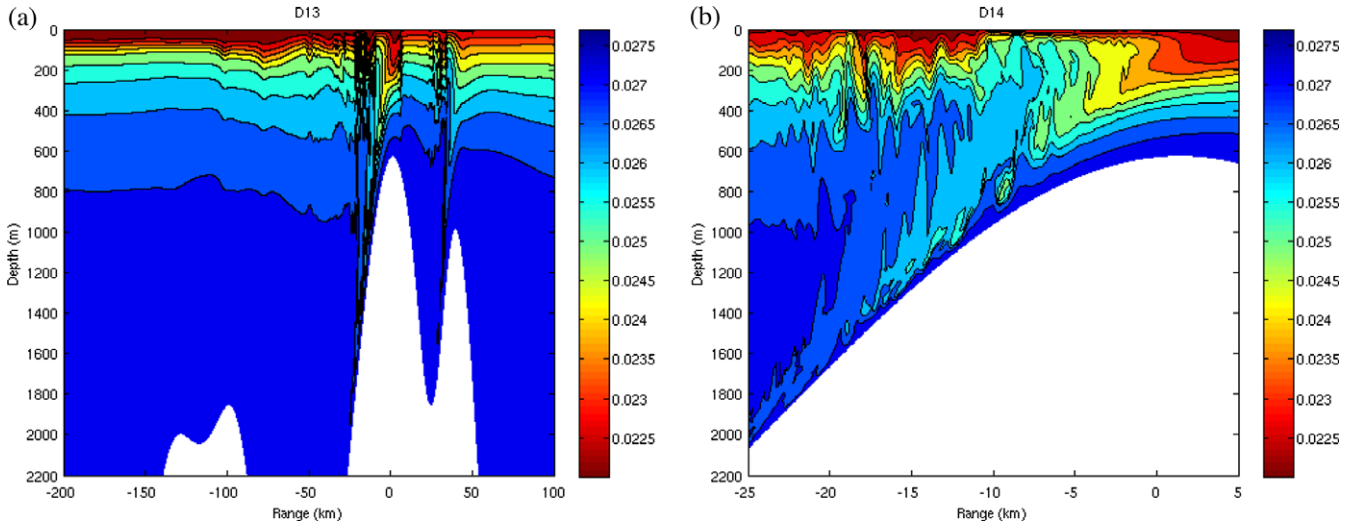

Fig. 9. Density field for case 3 (strong tidal forcing): (a) $t = 13$ h and (b) zoom in on Kelvin–Helmholtz instabilities over the taller crest of the second sill at $t = 14$ h.

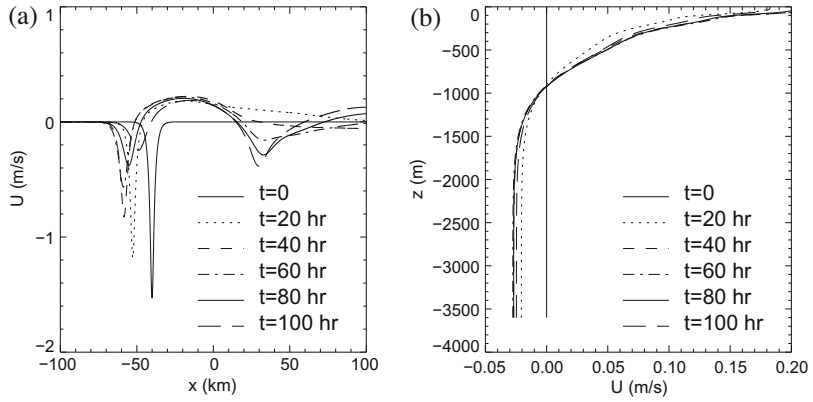

Fig. 10. Evolution of a single exact internal solitary wave under the influence of rotation. West stratification is used. Initial wave amplitude is 117 m. Simulation done in a reference frame moving with speed 2.8 m s^{-1}, slightly less than the initial propagation speed of the wave begin 3.02 m s^{-1}: (a) wave induced horizontal velocity at the surface every 20 h and (b) vertical profiles of the wave induced horizontal velocity at $x = -20$ km, a location behind the leading ISW.

ISW train at about −300 km (Fig. 13(b)). This wave train is significantly larger than in case one (see Fig. 6(e)). This is somewhat surprising as this ISW train evolves from the depression which is at $x = -50$ km at $t = 13$ h. This depression, which is on the lee of the tall sill, is smaller in case 4. The larger ISW train appears because of an interesting interaction between the wave generation process at the two sills. The westward propagating depression arrives at the smaller sill when the barotropic current has reversed direction, at which point its amplitude is increased. The presence of the eastward background current enhances this process. On the east side of Luzon Strait the ISW train at 300 km is similar to that in case 1.

In case of a westward current, case 5, the flow over the sills at $t = 13$ h is enhanced by the background current (Fig. 14). Consequently the depression in the lee of the taller sill is larger and is subject to intense breaking. To the left of the depressions at the taller sill, structures reminiscent of square waves are evolving. At 38 h, there are more solitary waves in the eastward propagating wave train than in the case of no background current. This is due to the much larger depression formed in the lee of the tall sill during westward tidal flow.The westward propagating ISW train at $x = -200$ km is smaller: a westward background current has the opposite effect to an eastward one.

3.5. Dependence on initial density field

The final two cases use initial density fields which are horizontally uniform, using either the density fit on the west side of the strait (ρ_w, case 6) or on the east side (ρ_e, case 7). For both of these cases the base tidal forcing T_2 is used and there are no background currents.

The predicted density field at 66 h using ρ_w is shown in Fig. 15(a). The solitary wave train distributions to the left of the sills are similar to those of case 1 shown in Fig. 6(f). To the right of the sills the solitary waves have not propagated as far from the sill, indicative of smaller phase velocities. Amplitudes of the solitary waves, on the right side, tend to be smaller that those in Fig. 6(f).

The predicted density field at 66 h using ρ_e is shown in Fig. 15(b). To the right of the sills the density distribution is similar to case 1. To the left the density distributions differ. In Fig. 15(b) the solitary wave trains have propagated further to the west, indicative of a larger phase speed, and the second train from the left has a different structure in the two cases (compare Figs. 15(b) and 6(f)). In case 7 the second solitary wave train has fewer distinct solitary waves and the first two solitary waves in the wave train have larger amplitudes than those in the corresponding waves train from case 1.

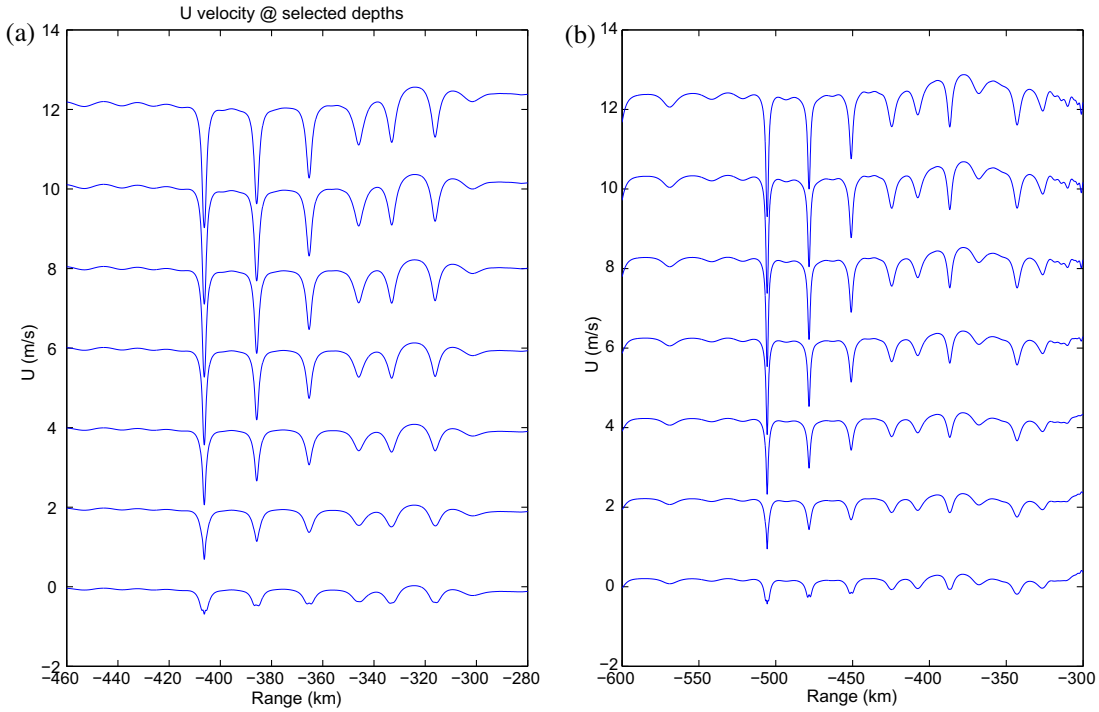

Fig. 11. Profiles of horizontal velocity for case 1 at selected depth as function of range. From top to bottom depths in m are: 50, 100, 150, 200, 250, 300, and 350. Vertical scale is for depth 350 m with others offset by 2 $m s^{-1}$ as surface is approached. (a) $t = 60$ h and b) $t = 68$ h.

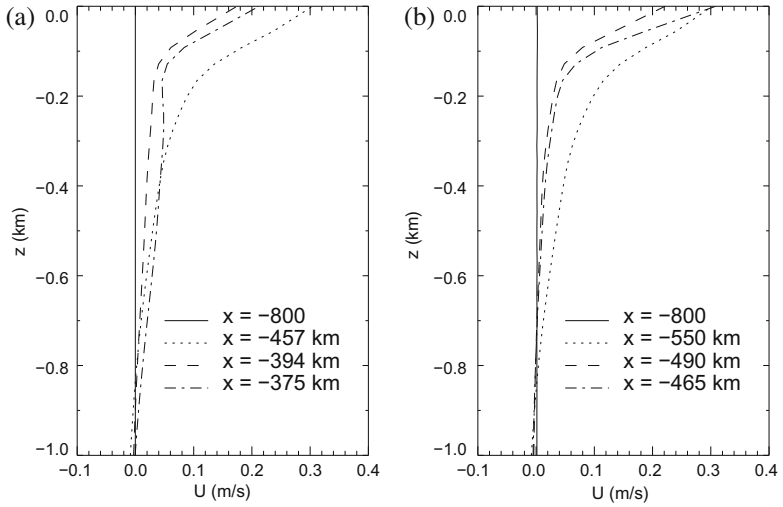

Fig. 12. Vertical profiles of horizontal velocity at selected ranges: case 1: (a) $t = 60$ h and (b) $t = 68$ h.

We attribute the changes in the ISWs generated in these two cases to the fact that density ρ_w has weaker stratification than ρ_e at the depth of the largest sill (600 m).

3.6. Wave energetics

To explore the energetics all the cases except case 5 were rerun at double the resolution, using a resolution of 35 m in the central domain and 200 grid points in the vertical. Fig. 16 shows the vertically integrated energy density E for five of the seven cases at $t = 55$ h. Here

$$E = \int_{-H}^{0} (E_k + E_a)\, dz, \tag{6}$$

where E_k is the baroclinic kinetic energy density and E_a is the available potential energy density Lamb, 2007. For the available potential energy calculation we use the initial density field on each side of the sill as the reference density, which is appropriate for calculating the available potential energy in an infinite domain Lamb, 2008. The energy is calculated in the regions $x < -180$ km and $x > 150$ km. We do not calculate the energy over the sill where the initial density varies horizontally, a reference density is hard to define, and where the sill topography complicates matters. From Fig. 16 it is clear that the internal solitary waves contain most of the energy in the internal wave field. By integrating horizontally across a wave feature we can determine its total energy. Values for selected waves are provided in Table 4. For case 1 the leading wave at $x = -350$ km has an energy of 3.7 $GJ m^{-1}$ (i.e., GJ per m along

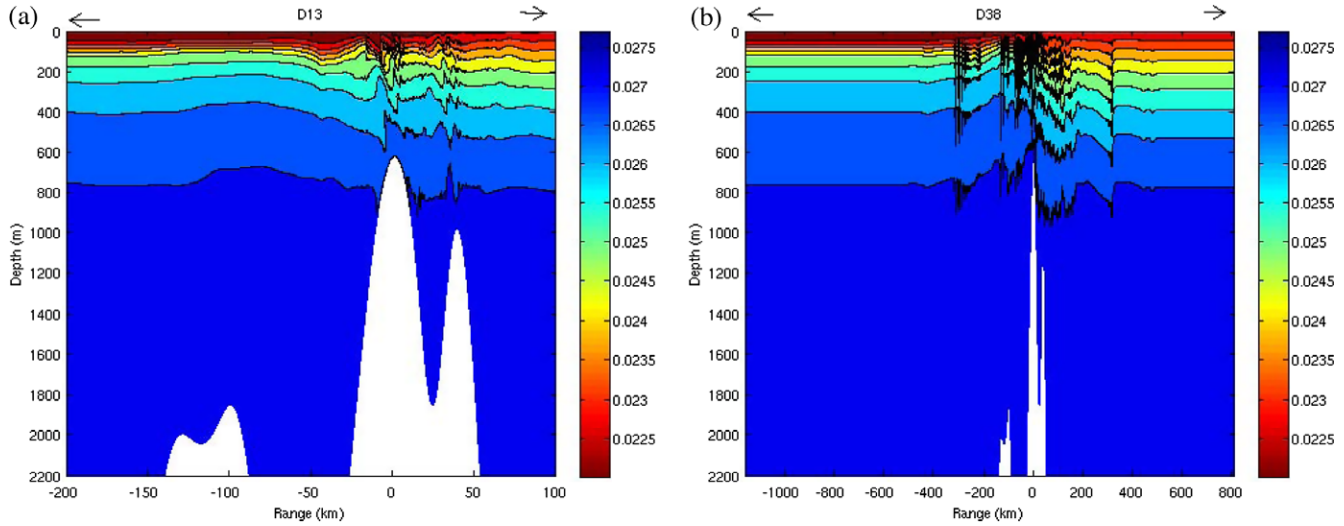

Fig. 13. Effects of a steady eastward background current (case 4) on the density field: (a) $t = 13$ h and (b) $t = 38$ h. Arrows on left side of figures indicate direction of tidal flow. Arrows on right side of figures show direction of background current.

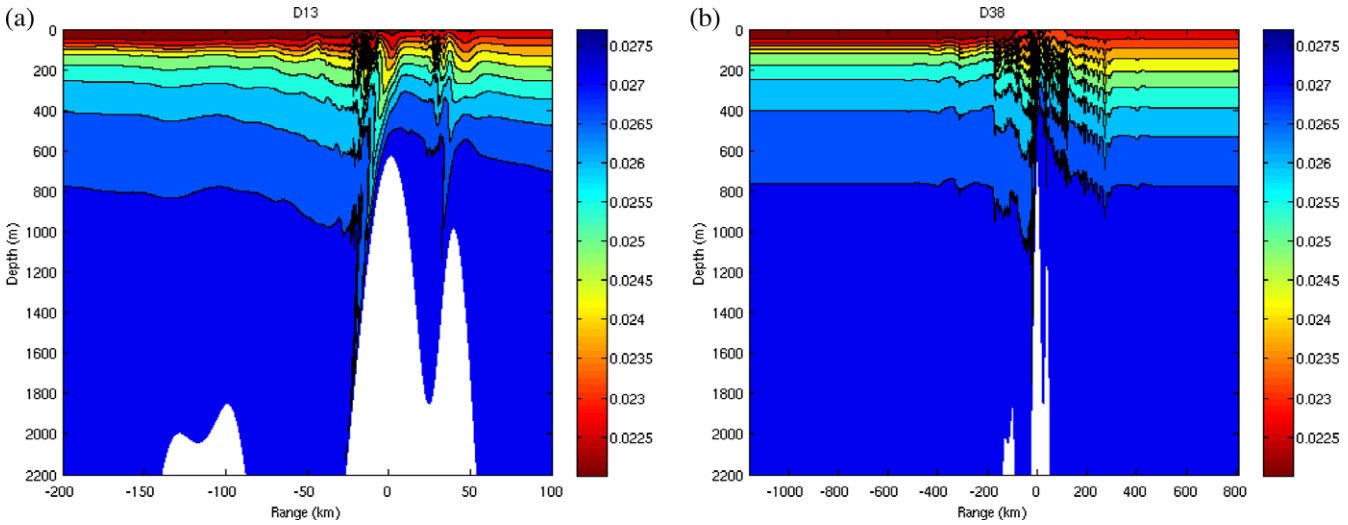

Fig. 14. Effects of a steady westward background current (case 5) on the density field: (a) $t = 13$ h and (b) $t = 38$ h.

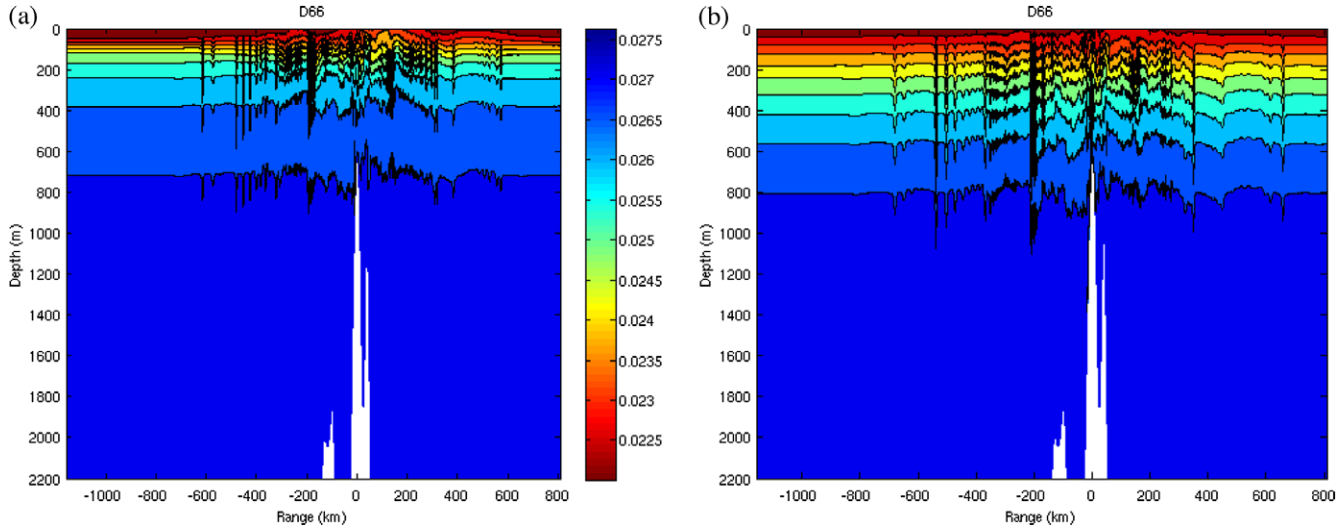

Fig. 15. Density fields for cases with horizontally uniform initial density field: (a) case 6 (west density fit) at $t = 66$ h and (b) case 7 (east density fit) at $t = 66$ h.

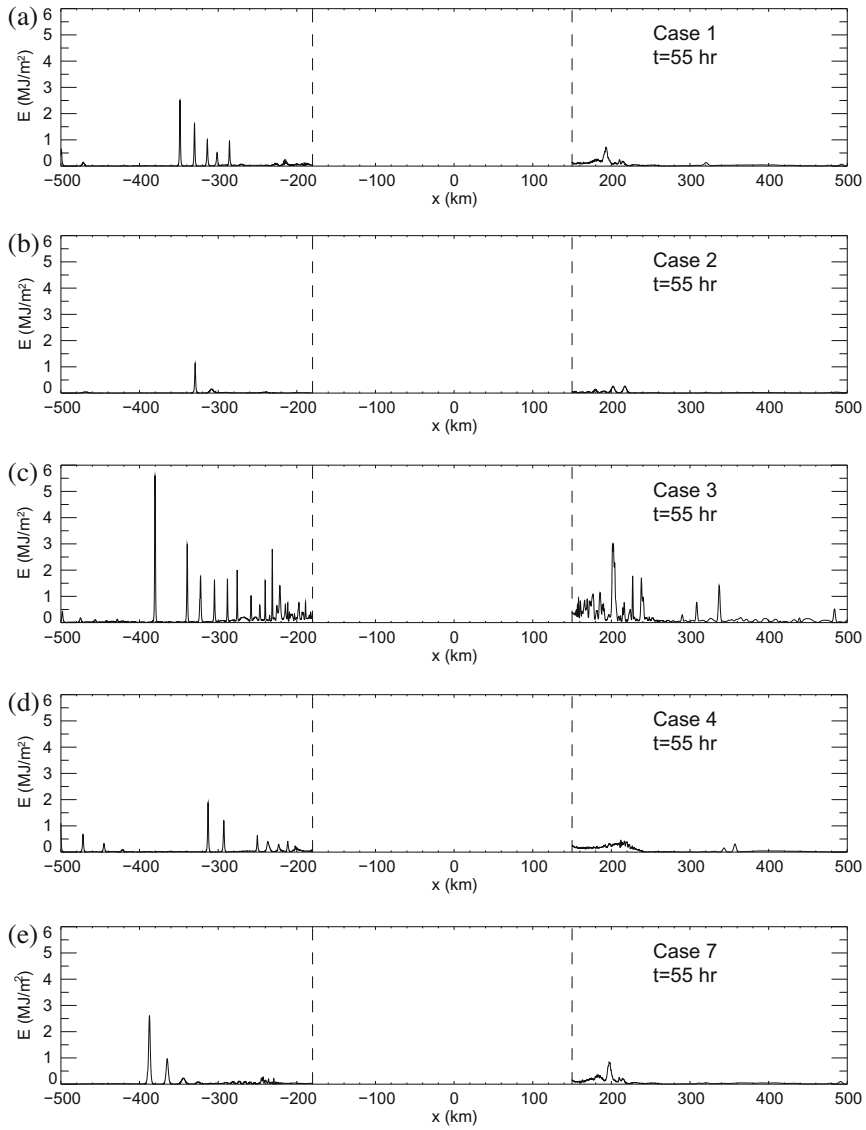

Fig. 16. Vertically integrated energy densities (kinetic plus available potential energy) at $t = 55$ h. Values calculated in regions $x < -180$ km and $x > 150$ km (indicated by vertical dashed lines): (a) case 1, (b) case 2, (c) case 3, (d) case 4 and (e) case 7.

the wave crest in the y-direction) while for case 2 it is 1.8 GH m^{-1}. For comparison Klymak et al. (2006) reported on a wave in the South China Sea with an energy of 1.8 GJ m^{-1}. Comparing case 6, which uses stratification ρ_w, with case 1 there is little difference in the energy of the first two solitary waves however the packet as a whole contains less. The first two solitary waves in case 7, which uses the eastward stratification, contain much more energy, although the full packet, which has one less ISW at this time, contains only slightly more energy.

Fig. 17 shows the baroclinic energy fluxes at $x = -200$ km as a function of time for case 1. Shown are the linear energy fluxes

$$W(x,t) = \int_{-H}^{0} u'p'\,dz, \tag{7}$$

where u' and p' are the baroclinic horizontal velocity and pressure perturbations (the difference between the pressure and the background pressure minus the surface pressure perturbation), the kinetic energy flux

$$KE_f(x,t) = \int_{-H}^{0} u'E_k\,dz, \tag{8}$$

Table 4
Baroclinic energy (kinetic plus available potential) in internal solitary waves at $t = 55$ h. E_1 is energy in the leading westward solitary wave in the first large amplitude wave packet. x_1 is its location. E_2 and x_2 are values for the second wave. E_{packet} gives the energy in the wave packet, with the number of waves included in brackets.

Case	E_1 (GJ/m)	x_1 (km)	E_2 (GJ/m)	x_2 (km)	E_{packet} (GJ/m)
Energetics					
1	3.7	−350	2.5	−330	12.2 (5)
2	1.8	−330	1.0	−310	3.2 (3)
3	9.0	−375	5.1	−340	27.0 (6)
4	2.9	−310	2.0	−290	11.0 (6)
6	3.4	−350	2.5	−330	9.7 (5)
7	7.3	−390	3.4	−65	13.0 (4)

and available potential energy flux

$$APE_f(x,t) = \int_{-H}^{0} u'E_a\,dz. \tag{9}$$

The sum of the kinetic and available potential energy fluxes in the solitary waves is comparable to the linear energy flux, while in the leading wave in the second wave packet (at $t = 67$ h) the

kinetic energy flux actually exceeds the linear energy flux. The fluxes are generally negative because the waves are propagating in the negative x-direction. A vertical expansion of the fluxes is shown in Fig. 18. Between the solitary wave packets the linear energy flux makes the dominant contribution to the total energy flux. The linear energy flux is always negative; however, the kinetic and available potential energy fluxes, for a leftward propagating wave (as here), are negative below the wave troughs and positive below the wave crests.

An important problem is that of the conversion rate of barotropic to baroclinic energy by tide-topography interaction Niwa and Hibiya, 2001, 2004, 2006, 2007. The time-averaged baroclinic westward energy fluxes $\langle W\rangle$, $\langle KE_f\rangle$, $\langle APE_f\rangle$ and their sum $\langle E_f\rangle$ at $x = -200$ km are shown in Fig. 19. Here the average of F is defined as

$$\langle F(x,t)\rangle = \frac{1}{2\tau_{M2}}\int_{t-2\tau_{M2}}^{t} F(x,t')\,dt'. \tag{10}$$

The averaging period is close to one period of the K_1 and O_1 tidal constituents. Values of the eastward and westward average total energy fluxes $\langle E_f\rangle$ at $x = \pm 200$ km, along with net energy flux (eastward plus westward), at $t = 60$ h are given in Table 5. The contribution to the total provided by the linear energy flux is also given. This value is high, ranging between 94% and 96% on the eastward side of the sill. On the westward side there is considerable variation. In all cases the linear energy flux dominates the tidally averaged values, contributing 96%, 80% and 72% of the total energy flux for cases 2, 1 and 3 (weak, medium and strong forcing), a reflection of its dominance outside of the large solitary waves. The eastward energy flux is always higher than the westward energy flux, with the largest difference (55%) occurring in case 2, the weakly forced case. For case 7, which is identical to case 1 except that the eastward stratification is used on both sides of the sills, both the eastward and westward fluxes are larger than for case 1. The eastward flux is 12% larger than the westward flux compared to 23% higher in case 1. For case 6, which uses the westward stratification, the eastward and westward energy fluxes are smaller than in case 1.

Because our numerical model uses a rigid lid there are no barotropic waves present. To estimate the barotropic to baroclinic conversion rate in our simulations we use the barotropic energy flux that would be present in barotropic waves with the same horizontal velocity amplitude as our prescribed tidal forcing. We have not

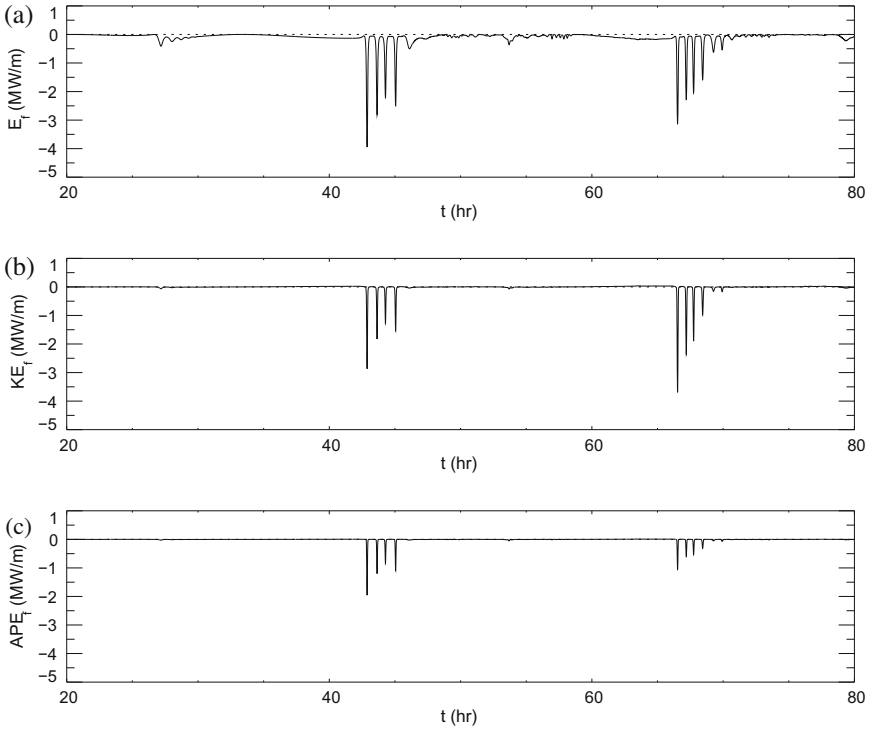

Fig. 17. Energy fluxes at $x = -200$ km for case 1: (a) linear energy flux, (b) kinetic energy flux and (c) available potential energy flux.

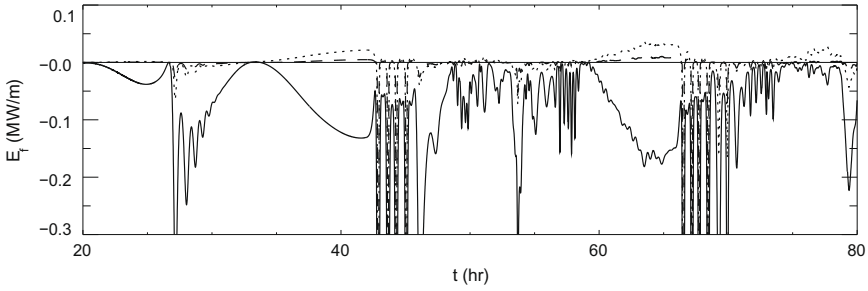

Fig. 18. Energy fluxes at $x = -200$ km for case 1: Linear energy flux (solid curve); kinetic energy flux (dotted curve); available potential energy flux (dashed line).

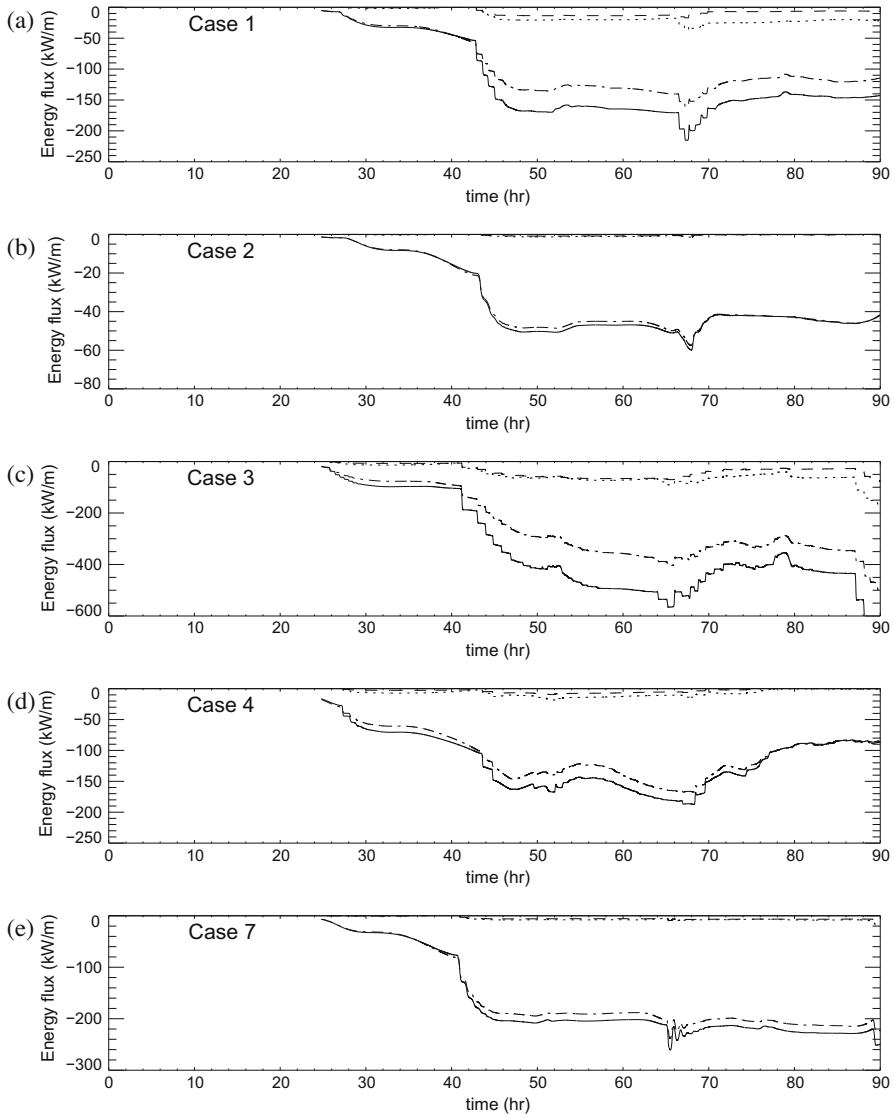

Fig. 19. Time averaged energy fluxes at $x = -200$ km. Values at time t are fluxes averaged over time interval $(t - \tau_{av}, t)$ where the averaging time τ_{av} is two M_2 tidal periods: (a) case 1, (b) case 2, (c) case 3, (d) case 4 and (e) case 7. Dash-dot: linear energy flux, dots: kinetic energy flux, dashed: available potential energy flux and solid: total.

Table 5
Averaged baroclinic energy fluxes at $x = \pm 200$ km. Numbers in brackets are percentage contributed by the linear energy flux. Final column gives total baroclinic energy flux as a percentage of the barotropic energy flux (see text).

Case	Westward (kW/m)	Eastward (kW/m)	Total (kW/m)	Total (% barotropic)
Average energy fluxes				
1	165(80)	204(96)	369	5.8
2	47(96)	73(95)	120	8.3
3	495(72)	643(96)	1138	3.6
4	160(88)	181(94)	341	5.4
6	141(82)	177(98)	318	5.0
7	200(93)	224(95)	424	6.7

estimated the amount of energy dissipated over the sill due to the nature of the simulations we have done, which are 2-dimensional inviscid simulations that cannot accurately simulate energy dissipation in breaking waves over the sill.

Consider a barotropic wave with horizontal current

$$U = a\sin(kx - \omega t). \tag{11}$$

From the continuity equation we have

$$\eta_t + HU_x = 0, \tag{12}$$

from which we find the free surface displacement is

$$\eta = a\frac{Hk}{\omega}\sin(kx - \omega t). \tag{13}$$

The hydrostatic pressure perturbation associated with the barotropic wave is $p_b = \rho_0 g\eta$, and its contribution to the (vertically integrated) barotropic energy flux is

$$\int_{-H}^{0} Up_b\,dz = \rho_0 g a^2 H^2 \frac{k}{\omega}\sin^2(kx - \omega t). \tag{14}$$

Averaging over a tidal period gives the tidally averaged barotropic energy flux

$$E_{fb} = \frac{1}{2}\rho_0 g a^2 H^2 \frac{k}{\omega}. \tag{15}$$

Given the wave frequency ω and Coriolis parameter f the wave number k is obtained from the dispersion relation $\omega^2 = f^2 + gHk^2$. Treating each tidal constituent independently,

for case 1 we obtain barotropic energy fluxes of 2800, 2370, and 1110 kW m^{-1} for the M_2, K_1 and O_1 constituents for a total of 6280 kW m^{-1}. The conversion rates for five cases are given in Table 5. In particular, for cases 2, 1 and 3 (weak, intermediate and strong forcing) the conversion rate is 8.3%, 5.8% and 3.6% respectively. These values need to be taken with caution as they are from idealized inviscid 2-dimensional simulations. Mixing and energy dissipation over the sill in the ocean is likely quite different. Jan et al. (2008) conducted 3-dimensional numerical simulations of the internal wave generation process in Luzon Strait using the hydrostatic Princeton Ocean Model. Their simulations used a horizontal resolution of about 10 km, 300 time coarser than ours. They estimated that about 25% of the barotropic energy is transfered to baroclinic waves of which a bit more than half is radiated away by internal waves. These latter values are about 50% higher than ours for the weakly forced case.

4. Dispersion

To illustrate the temporal evolution of the westward propagating wave trains, the evolution of the $\sigma_\theta = 24.5$ kg m^{-3} isopycnal to the left of the large sill is illustrated for case 1 in Fig. 20(a), for times between 50 and 74 h at 2 h intervals. At 50 h there are two solitary wave trains with wave fronts at $x = -450$ and -280 km. At 60 h the second train has propagated to -400 km. At this time a third, small amplitude wave train is starting to form at -280 km and a fourth, large amplitude wave train is forming at -110 km. By 66 h the third wave train is at -320 km and exhibits two distinguishable solitons of small amplitudes followed by a packet of small amplitude short waves with wavelengths of about 4 km. The fourth wave train is now at -175 km. By 74 h there is a small wave train at -700 km, followed by a large solitary wave train at -575 km, a small solitary wave train at -390 km and a large wave train at -280 km. The second wave train is overtaking the leading wave train. At $t = 74$ h the leading wave of the second train has almost caught up with the fourth wave in the leading wave train. By $t = 83$ h it has caught up with the third wave (not shown). The large solitary wave trains are generated about 24 h apart, with the small solitary wave train appearing about 12 h after the large one, consistent with observations Ramp et al., 2004.

A striking feature of the second solitary wave train (the first large amplitude wave train) is that apart from the leading two waves, the amplitudes of the individual waves vary considerably as the wave train evolves (Fig. 20(b)). At $t = 50$ h the first four waves are rank ordered, with the largest wave in front. The fifth wave has an amplitude between those of the third and fourth waves, breaking the rank ordering. Two hours later the fifth wave is significantly larger than the fourth. The fourth wave decays rapidly after which the fifth wave also decays. The sixth wave, which was very tiny at $t = 50$ h, grows and becomes larger than the fourth and fifth waves by $t = 64$ h. As time progresses from 50 to 74 h the distance between the solitary waves increases. In contrast the amplitude of the first solitary wave in the wave train remains approximately constant in time while the second one decreases somewhat in amplitude. The third and fourth solitary waves show an appreciable decrease in amplitude in relation to the first and second solitary waves. The tendency for the train is to retain the first and second solitary waves as they propagate while the following waves decay. Hence the wave train appears to be evolving towards a two-solitary wave train.

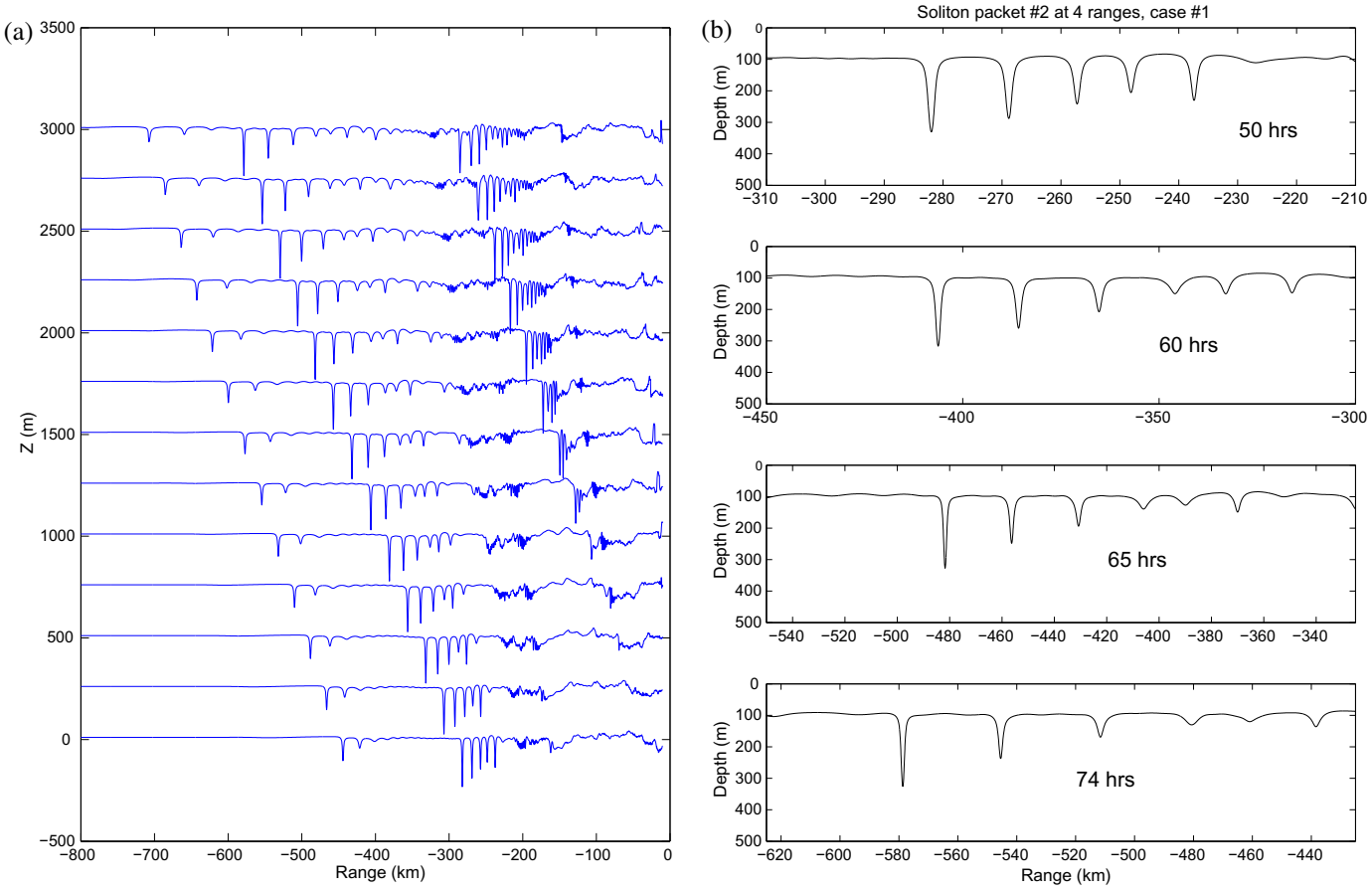

Fig. 20. The $\sigma_\theta = 24.5$ kg m^{-3} isopycnal at different times for case 1. From bottom to top time increases by 2 h. Bottom is at 50 h. Vertical scale is offset by 250 m: (a) wave field to the left of the tall sill. Isopycnals shown at 2 h intervals between 50 and 75 h and (b) a zoom of the second solitary wave train at $t = 50, 60, 65$ and 74 h.

The half width (L) of the ISWs is defined as half the width of the trough at half amplitude. The full widths ($2L$) and amplitudes of the first three solitary waves in the second train are plotted in Fig. 21(a) at various times. At 50 h, the full widths range from about 1.26 km, for the first solitary wave, to 1.29 km, for the third solitary wave. The corresponding amplitudes vary from 235 to 155 m. At 74 h, the full widths range from 1.37 km, for the first solitary wave, to 2.65 km, for the third one with the corresponding amplitudes decreasing from 230 to 75 m. The first ISW retains its large amplitude, of around 230 m, while the third wave's amplitude decreases from 155 to 75 m.

Case 1 was initialized with the horizontally varying density field shown in Fig. 5b. Cases 6 and 7 were initialized using the west and east side profiles respectively. The full width and amplitude dispersion diagram for these three cases are shown in Fig. 21(b) at 66 h. The amplitude of the first ISW remains large among the three cases. The dispersion curves for cases 1 and 6, which have the same stratification to the west of the sill, are similar. The dispersion curve for case 7 is very different, the waves being roughly three times wider and about 30–50% larger.

The phase speeds of the westward propagating solitary waves in the first large amplitude solitary wave train in cases 1 and 7 are given in Table 6. We tracked the trough of the first three solitary waves at 50, 60, 65, and 74 h versus range and least-square fitted a straight line. The slope of the fitted line yielded the phase speeds listed in Table 6. The phase speeds for the first, second, and third solitary waves varied from 3.44 to 2.95 $m s^{-1}$ in case 1 and were slightly larger, ranging from 3.8 to 3.2 $m s^{-1}$, in case 7. This is due in part to the larger amplitudes.

For comparison, plots showing the properties of exact nonlinear internal solitary waves, for which rotational effects are ignored, are shown in Fig. 22 Lamb, 2002. These show that for a given wave amplitude, in the absence of rotational effects, waves in the eastward stratification have larger phase speeds, smaller maximum wave-induced currents and are narrower. Comparisons of the half width of the 24.5 isopycnal and the isopycnal undergoing maximum vertical displacement indicate some variation in half widths with depth. The exact internal wave full widths ($2L$) for the western stratification are close to those for case 1 shown in Fig. 21(b).

Comparisons of weakly nonlinear KdV with extended KdV, Miyata, Benjamin-Ono, Choi and other models exist in the literature Brandt et al., 1997, 1999, 2005. The comparisons encompass models and data. What emerges is that as the degree of nonlinearity is increased, there is less decrease of wavelength as a function of amplitude. Fully nonlinear models Choi and Camasa, 1999 exhibit less decrease in wavelength versus amplitude relative to KdV or extended KdV. KdV and extended KdV models exhibit a decrease in wavelength as a function of amplitude that is larger than shown by nonlinear models Brandt et al., 1997. The difference in decrease of wavelength as a function of amplitude between the extended KdV and nonlinear models can be as large as 50% less for extended KdV Brandt et al., 1997.

Table 6
Simulated phase speeds

Solitary wave	Case 1 phase speed ($m s^{-1}$)	Case 7 phase speed ($m s^{-1}$)
1	3.44	3.80
2	3.21	3.46
3	2.95	3.19

5. Comparisons with measurements and analytical solutions

At the ASIAEX site large amplitude solitary waves were observed. Duda et al. (2004) analyzed thermistor chain data at mooring S7 (see Fig. 1), located in a depth of 350 m. They fitted the data to a KdV solitary wave which has the form

$$\eta(x,t) = a\,\mathrm{sech}^2[(x-ct)/L], \tag{16}$$

where a is the amplitude, L the half width (slightly different from the definition of the half width used above) and c the propagation speed.

We calculated the half widths from the data assuming a phase speed of 1.5 $m s^{-1}$ Duda et al., 2004. We analyzed the model predictions at 74 h that approximately corresponds to the arrival of a large amplitude solitary wave train at the ASIEAX experimental site. Such a train represent possible solitary waves before shoaling to the observational depth of 350 m.

The observed waves have amplitudes ranging from 100 to 155 m and full widths from about 800 to 700 m. These are compared with the modelled waves, for cases 1 and 7, in a water depth of 3665 m in Fig. 23, where the full widths (2 L) are plotted. Klymak et al. (2006) observed solitary waves with an amplitude of 170 m and a half width of 3 km in the deep central basin of South China Sea. These measurements are also included in Fig. 23. The dispersion diagram

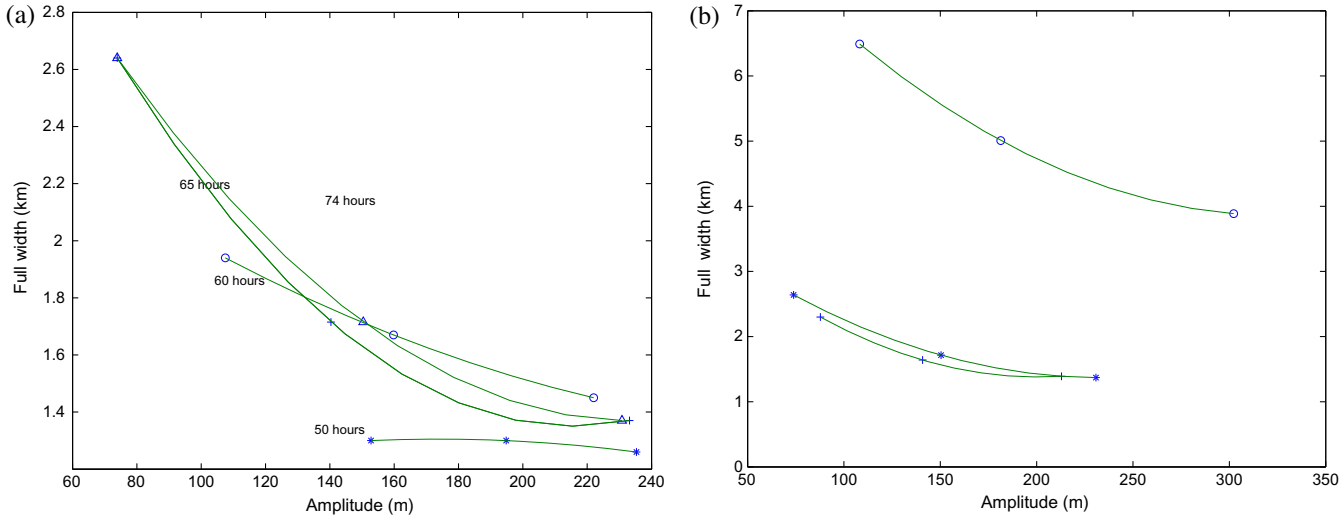

Fig. 21. Dispersion curves: wave full width (2 L) versus amplitude: (a) leading three solitary waves from case at $t = 50$ (star), 60 (circle), 65 (plus), and 74 (triangle) h. Lines are least squares polynomial fits and (b) comparison of leading three solitary waves for cases 1 (star), 6 (plus) and 7 (circle) at 65 h.

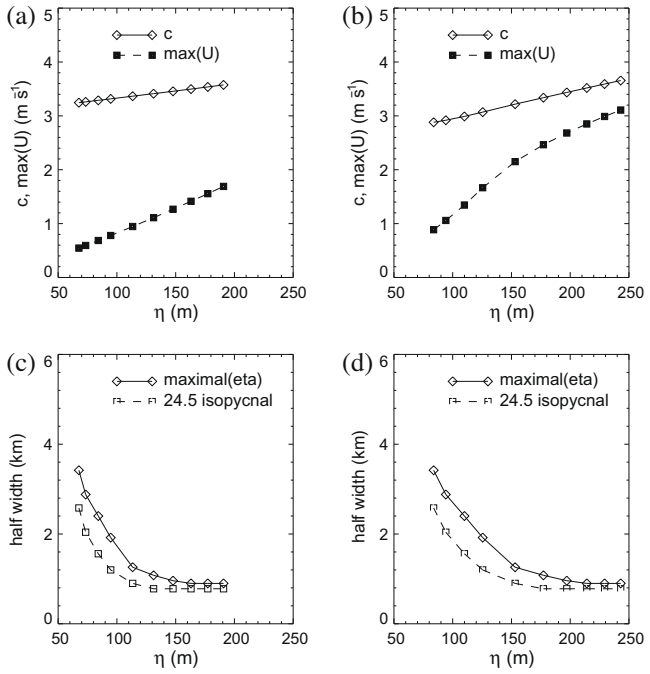

Fig. 22. Properties of exact internal solitary waves in nonrotating fluid in the absence of a background current. (a and b): propagation speed and maximum wave induced current as function of wave amplitude in eastern (a) and western (b) stratification. (c and d): wave half width (L) as a function of wave amplitude in eastern (c) and western (d) stratifications. Solid: half width of isopycnals undergoing maximum displacement. Dashed: half width of $\sigma_\theta = 24.5$ isopycnal.

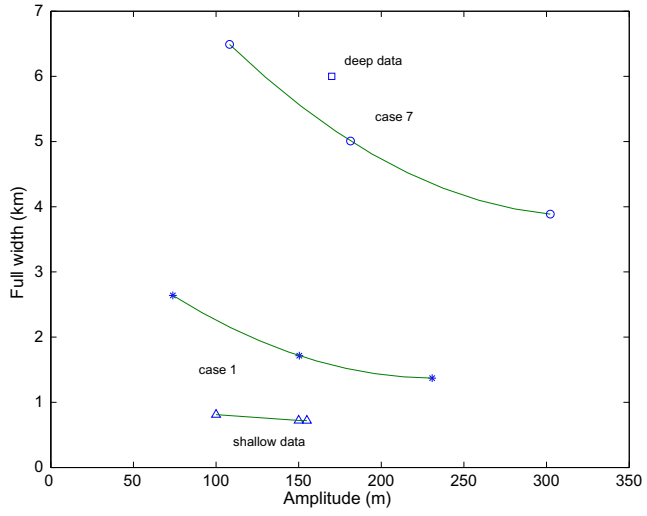

Fig. 23. Dispersion of full width (2L) versus amplitudes for case 1 (star), case 7 (open circle), thermistor chain data (triangle) at mooring S7 in 350 m depth and deep water measurements west of Luzon Strait (square). Lines indicate a least square polynomial fit.

spans deep and shallow water regimes. The shallow water regimes contains the initial stages of shoaling that reduce the phase speeds and half widths. The deep water measurements of Klymak et al. (2006) are in much better agreement with the simulation using the eastern stratification. Vlasenko et al. (2005) studied dispersion changes with a nonlinear model as stratification is varied. He observed changes in predicted wavelengths as a function of amplitude as the stratification is changed from a sharp thermocline to a diffuse thermocline. A thermocline with large depth variations resulted in larger wavelengths as a function of amplitude. This is a similar behavior to case 7 in Fig. 23 as compared with case 1.

The phase speeds at the ASIAEX site are estimated to range from about 1.2 to 1.8 m s^{-1} Duda et al., 2004. Out in the deep areas of South China Sea, larger phase speeds are observed. Analysis of WISE data indicate phase speeds of 3.4 m s^{-1} and amplitudes ranging from about 140 to 220 m Ramp, 2006 while the wave reported by Klymak et al. (2006) had a phase speed of about 2.9 m s^{-1}.

The model predictions for case 1 at a range of amplitudes from 100 to 170 m exhibit full widths that are closer to the shallow water measurements than the deepwater measurements (Fig. 23). The model predictions for case 7 show a dispersion curve that for an amplitude of 170 m is close to the measured full width of 6 km in deep water. Case 7 is initialized from the east side density, which is more strongly stratified at the depth of the sill in Luzon Strait, than is the west side density.

For high and low tidal forcing, cases 1 and 2, we fitted a sech^2 shape to the first soliton of the second solitary wave train at 74 h. The parameters of the fit are listed in Table 7 for cases 1 and 2.

For case 1 the sech^2 fit to the 25.05 isopycnal is shown in Fig. 24. This is an isopycnal located near the mid pycnocline. The two curves agree very well. The deviation on the top right represents the predicted isopycnal's gradual return to equilibrium. In the model simulation the waves are superimposed on an internal tide, not on the initial density field, and are modified by rotational effects. In both cases 1 and 2, using high and low tidal forcing, the sech^2 shape of the analytical KDV solution fits the simulated waves quite well, suggesting that the weakly-nonlinear KdV analytical sech^2 solution is a fair approximation for this particular physical situation.

Table 7
Internal wave characteristics based on the $\sigma_\theta = 25.06$ isopycnal.

Case	a (m)	$2L$ (km)	c (m s^{-1})
1	240	1.49	3.44
2	155	1.74	3.22

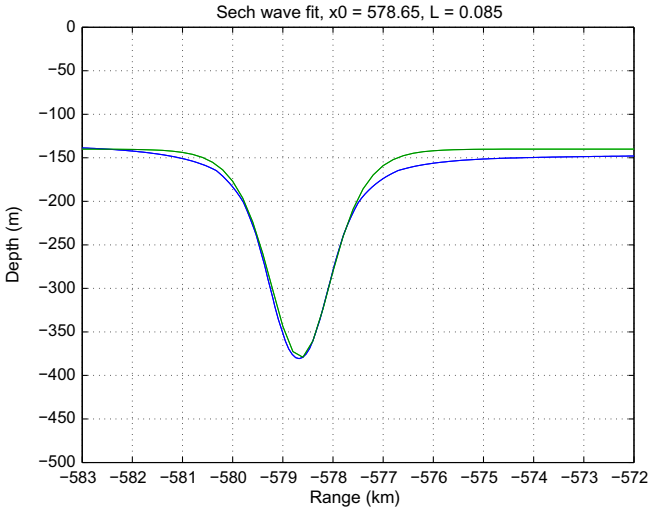

Fig. 24. Sech^2 analytical KdV solution fit (green curve), to the $\sigma_\theta = 25.05$ isopycnal at 74 h in case 1 (blue curve). (For interpretation of references in color in figure legends, the reader is referred to the web version of this article.)

Duda et al. (2004) fitted a sech^2 to thermistor chain data at an ASIAEX mooring site where the ocean depth is 350 m. The fits follow the amplitudes of the data. The data, however, tends to be wider than the fits. Some measurements indicate a flatter peak. The start of shoaling effects can be expected at a depth of 350 m. The disagreement between measured isotherms and fitted shapes could be due to the beginning of shoaling effects.

A sech^2 fit to the data in the central basin of South China Sea by Klymak et al. (2006) also showed good agreement between the weakly-nonlinear KdV solitary waves and the observed waves. Klymak et al. (2006) concluded that the sech^2 shape tends to be maintained over a distance of 60 km. In our model predictions, the first solitary wave in the large amplitude wave trains that have evolved to a mature stage, approximately maintain their amplitude as they propagate while the full width increases by less than 10%.

6. Conclusion

In the Luzon Strait region the barotropic tide predominantly consists of K1, M2, and O1 components. Studies with a nonhydrostatic model show that barotropic tidal motion over the Luzon Strait sills result in the generation of depressions. These depressions propagate away from the sill region, their leading edge steepens through nonlinear effects, and disintegration into solitary waves occurs through frequency and amplitude dispersion.

The magnitude of the tidal components affect the amplitude of the generated depression, the evolution of solitary waves and the subsequent structure of the solitary wave trains. A reduction in tidal forcing can result in no solitary wave trains appearing, or solitary wave trains with smaller amplitudes and fewer solitary waves. Correspondingly, an increase in the tidal forcing results in more solitary waves with larger amplitudes. Higher tidal amplitudes can lead to Kelvin–Helmholtz instabilities at the taller Luzon Strait sill.

A tuned set of parameters yielded large amplitude solitary wave trains about every 24 h with smaller amplitude solitary wave trains in between, about 12 h after the large amplitude solitary wave trains, in agreement with observations Ramp et al., 2004. An interesting phenomena occurred as the ISW trains evolved. The first solitary wave in the large-amplitude wave trains maintained its amplitude as it propagated towards the ASIAEX site. The second solitary waves attenuated somewhat while the remaining waves attenuated appreciably. The result was a train with two solitary waves arriving at the ASIAEX site. The cause of this phenomena will require further study.

The predicted amplitudes and full width dispersions were compared with ASIAEX thermistor chain measurements of Duda et al. (2004) at a mooring located in a depth of 350 m and the measurements of Klymak et al. (2006) in the deep central area of the South China Sea. The model predicted dispersion of amplitude and full width was bounded by the measured dispersion in shallow and deep areas of South China Sea. A model prediction with a density profile that contained more density change at the 600 m sill location, as provided by the stratification on the eastern side of the sill, resulted in soliton amplitudes and full widths that were closer to the deep water measurements of Klymak et al. (2006). The predicted deep water phase speeds, about 3.44 m s^{-1} for first solitary wave, were in the range of the Klymak et al. (2006) and Ramp (2006) observed values of 2.9 and 3.4 m s^{-1} respectively.

A sech^2 analytical KdV solution was fitted to the first ISW in the wave trains for large and small tidal forcing. The fit matched and was preserved as the soliton propagated westward towards China. The preservation of the sech^2 shape was also observed by Klymak et al. (2006) in the central South China Sea over a 60 km distance. This suggested that the weakly nonlinear KdV analytical sech^2 solution is a fair approximation for this particular physical situation.

A steady background current through the strait, such as the Kuroshio, affects the evolution and structure of solitary wave trains. The magnitude of the Kuroshio current is of the order of 1 m s^{-1} through Luzon Strait in a north eastwards direction. In a westwards direction there can be a steady flow of 0.1 m s^{-1} due to the Kuroshio or some other current. In our simulations we found that in the presence of an eastward current, the westward propagating depression can arrive at the smaller sill at a time when the barotropic current has reversed direction at which point its amplitude is increased. This results in a larger ISW train.

The location of the pycnocline and the stratification strength of the pycnocline region affects the generation, evolution and characteristics of solitary wave trains. At the depth of the higher sill, around 600 m, an increasing stratification leads to larger amplitude ISWs with larger phase speeds.

An analysis of the background current structure that the solitary waves encounter was undertaken. The variations of the u velocity component between solitons in a train was tracked. It was found that there is a distinct subsurface shear layer of increasing velocity in the vertical and horizontal.

The energetics of the ISW trains was also explored. To the west of the sills most of the wave energy is contained in the ISWs. In the ISWs the kinetic and available potential energy fluxes are comparable to the linear energy flux and in one wave the kinetic energy flux exceeded the linear energy flux. Outside the ISWs the linear energy flux dominates. Averaging over two semidiurnal tidal periods the linear energy flux was found to provide between 72% and 96% of the total energy flux. The energy fluxes were sensitive to barotropic tidal magnitude, initial density and background current. Increasing the barotropic tide, increased the internal wave fluxes but reduced the percentage of the energy that was transferred to radiating internal waves. For case 1, which used the intermediate tidal currencts, the leading wave at $x = -330$ km has an energy of 3.7 GJ m^{-1}. For the weakly forced case this wave had contained 1.8 GJ m^{-1}, the same value that Klymak et al. (2006) estimated for a wave observed in the South China Sea.

Estimates of the fraction of barotropic tidal energy transferred to radiating internal solitary wave energy were made. Conversion rates of 8.3%, 5.8%, and 3.6% were obtained for low, medium and high tidal forcing. In low resolution simulations using the hydrostatic Princeton Ocean model Jan et al. (2008) obtained conversion rates that were about 50% higher than value for the weakly forced case (8.3%). In their simulations approximately the same amount of energy was dissipated near the generation site. There is a need for high resolution 3-dimensional simulations to further explore this question.

Acknowledgments

This work was supported by the Office of Naval Research under PE 62435 N, with technical management provided by the Naval Research Laboratory. Lamb was supported by a grant from the Natural Sciences and Engineering Research Council of Canada. We thank Dr. Dong Ko for providing density profiles in Luzon Strait region. We thank Dr. Tim Duda for providing the analyzed ASIAEX data. Our thanks to Dr. Steve Ramp for communicating the result of WISE to us.

References

Apel, J.R., Holbrook, J.R., Tsai, J., Liu, A.K., 1985. The Sulu Sea internal soliton experiment. J. Phys. Oceanogr. 15, 1625–1651.

Brandt, P., Alpers, W., Backhaus, J.O., 1996. Study of the generation and propagation of internal waves in the Strait of Gibraltar using a numerical model and

synthetic aperture radar images of the European ERS1 satellite. J. Geophys. Res. 101, 14237–14252.
Brandt, P., Rubino, A., Alpers, A., Backhaus, W., 1997. Internal waves in the Strait of Messina studied by a numerical model and synthetic aperture radar images from ERS 1/2 satellites. J. Phys. Oceanogr. 27, 648–663.
Cai, S., Long, X., Gan, Z., 2002. A numerical study of the generation and propagation of internal solitary waves in the Luzon Strait. Oceanol. Acta 25, 51–60.
Chao, S.-Y., Ko, D.-S., Lien, R.-C., Shaw, P.-T., 2007. Assessing the west ridge of Luzon Strait as an internal wave mediator. J. Oceanogr. 63, 897–911.
Chin-Bing, S.A., Warn-Varnas, A., King, D.B., Lamb, K.G., Teixeira, M., Hawkins, J.A., 2003. Analysis of coupled oceanographic and acoustic soliton simulations in the Yellow Sea: a search for soliton-induced resonances. Math. Comput. Simul. 62, 11–20.
Chiu, C.-S., Ramp, S.R., Miller, C.W., Lynch, J.F., Duda, T.F., Tang, T.-Y., 2004. Acoustic intensity fluctuations induced by South China Sea internal tides and solitary waves. IEEE J. Oceanic Eng. 29 (4), 1249–1263.
Choi, W., Camasa, R., 1999. Fully nonlinear internal waves in a two-fluid system. J. Fluid Mech. 396, 1–36.
Duda, T.F., Lynch, J.F., Newhall, A.E., Wu, L., Chu, C.-S., 2004. Fluctuations of 400 Hz sound intensity in the 2001 ASIAEX South China Sea experiment. IEEE J. Oceanic Eng. 29 (4), 1264–1279.
Duda, T.F., Lynch, J.F., Irish, J.D., Beardsley, R.C., Ramp, S.R., Chiu, C.-S., Tang, T.Y., Yang, Y.-J., 2004. Internal tide and nonlinear wave behavior at the continental slope in the Northern South China Sea. IEEE J. Oceanic Eng. 29 (4), 1105–1130.
Garrett, C., Kunze, E., 2007. Internal tide generation in the deep ocean. Ann. Rev. Fluid Mech. 39, 57–87.
Helfrich, K., 2007. Decay and return of internal solitary waves with rotation. Phys. Fluids 19, 026601.
Jan, S., Lien, R.-C., Ting, C.-H., 2008. Numerical study of baroclinic tides in Luzon Strait. J. Oceanogr. 64, 789–802.
Klymak, J.M., Pinkel, R., Liu, C-T., Liu, A.K., David, L., 2006. Prototypical solitons in the South China Sea. Geophys. Res. Lett. 33, L11607. doi:10.1029/2006GL025932.
Klymak, J.M., Moum, J.N., Nash, J.D., Kunze, E., Girton, J.B., Carter, G.S., Lee, C.M., Sanford, T.B., Gregg, M.C., 2006. An estimate of tidal energy lost to turbulence at the Hawaiian Ridge. J. Phys. Oceanogr. 36, 1148–1164.
Lamb, K.G., 1994. Numerical experiments of internal waves generation by strong tidal flow across a finite amplitude bank edge. J. Geophys. Res. 99, 848–864.
Lamb, K.G., 2002. A numerical investigation of solitary internal waves with trapped cores formed via shoaling. J. Fluid Mech. 451, 109–144. doi:10.1017/S002211200100636X.
Lamb, K.G., 2007. Energy and pseudoenergy flux in the internal wave field generated by tidal flow over topography. Cont. Shelf Res. 27, 1208–1232. doi:10.1016/j.csr.2007.01.020.
Lamb, K.G., 2008. On the calculation of the available potential energy of an isolated perturbation in a density stratified fluid. J. Fluid Mech. 597, 415–427. doi:10.1017/S0022112007009743.
Liu, A.K., Holbrook, J.R., Apel, J.R., 1985. Nonlinear internal wave evolution in the Sulu Sea. J. Phys. Oceanogr. 15, 1613–1624.
Niwa, Y., Hibiya, T., 2001. Numerical study of the spatial distribution of the M_2 internal tide in the Pacific Ocean. J. Geophys. Res. 106, 22441–22449.
Niwa, Y., Hibiya, T., 2004. Three-dimensional numerical simulation of M_2 internal tides in the East China Sea. J. Geophys. Res. 109, C04027. doi:10.1029/2003JC00192.
Osborne, A.R., Burch, T.L., 1980. Internal solitons in the Andaman Sea. Science 208 (4443), 451–460.
Ramp, S., 2006. Private communication.
Ramp, S.R., Tang, T.Y., Duda, T.F., Lynch, J.F., Liu, A.K., Chiu, C.-S., Bahr, F.L., Kim, H.-R., Yang, Y.J., 2004. Internal solitons in the Northeastern South China Sea Part I: source and deep water propagation. IEEE J. Oceanic Eng. 29, 1157–1181.
Teixeira, M., Warn-Varnas, A.C., Apel, J., Hawkins, J., 2006. Analytical and observational studies of internal solitary waves in the Yellow Sea. J. Coastal Res. 22, 403–1416.
Vlasenko, V.I., 1993. Modelling of baroclinic tides in the shelf zone zone of Guinea. Izvestiya, Atmos. Oceanic Phys. 29 (5), 673–680.
Vlasenko, V.I., Ivanov, V.A., Krasin, I.G., Lisichenok, A.D., 1996. Study of intensive internal waves in the shelf zone of Morocco. Phys. Oceanogr. 7 (4), 281–298.
Vlasenko, V., Stashchuk, N., Hutter, K., 2005. Baroclinic Tides Theoretical Modelling and Observational Evidence. Cambridge University Press.
Warn-Varnas, A.C., Chin-Bing, S., Lamb, K., Teixeira, M., Hawkins, J., 2002. Yellow Sea internal solitary wave variability. In: NATO SACLANT Centre's Conference Proceedings. La Spezia, Italy.
Warn-Varnas, A.C., Chin-Bing, S.A., King, D.B., Hallock, Z., Hawkins, J.A., 2003. Ocean-acoustic solitary wave studies and predictions. Surv. Geophys. 24, 39–79.
Warn-Varnas, A.C., Chin-Bing, S.A., King, D.B., Hawkins, J.A., Lamb, K.G., Teixeira, M., 2005. Yellow Sea ocean-acoustic solitary wave modeling studies. J. Geophys. Res. 110, C08001.
Warn-Varnas, A.C., Chin-Bing, S.A., King, D.B., Hawkins, J.A., Lamb, K.G., Lynch, J.F., 2007. Winter PRIMER ocean-acoustic solitary wave modeling studies. IEEE J. Oceanic Eng. 32 (2), 436–452.
Yang, Y.-J., Tang, T.Y., Chang, M.H., Liu, A.K., Hsu, M.-K., Ramp, S., 2004. Solitary waves Northeast of Tung-Sha Island during the ASIAEX pilot studies. IEEE J. Oceanic Eng. 29 (4), 1182–1199.
Zhao, Z., Alford, M.H., 2006. Source and propagation of internal solitary waves in the Northeastern South China Sea. J. Geophys. Res. 111, C11012. doi:10.1029/2006JC003644.
Zhou, J.X., Zhang, X.Z., Rogers, P.H., 1991. Resonant interaction of sound wave with internal solitons in the coastal zone. J. Acoust. Soc. Am. 90, 2042–2054.